TÉCNICO LISBOA

Numerical investigation of the influence of operating conditions on a mild laboratory scale combustor

Mustafa Bal

Thesis to obtain Master of Science Degree in

Energy Engineering and Management

Supervisor: Prof. Pedro Jorge Martins Coelho

Examination Committee

Chairperson: Prof. José Alberto Caiado Falcão de Campos

Supervisor: Prof. Pedro Jorge Martins Coelho

Member of the Committee: Prof. Daniel Cardoso Vaz

September 2015

ABSTRACT

A novel low emission combustion technology called flameless oxidation emerged nearly two decades ago. In addition to low emissions, lower mean temperature and more uniform and stable combustion chamber conditions are achieved using flameless oxidation. Although the research has been done both experimentally and numerically, more research is needed to fully understand the mechanisms, benefits and drawbacks of the process.

In this study, the numerical simulation of a small scale cylindrical combustor operating in the flameless oxidation regime is carried out. The fuel (methane) is supplied to the chamber through 16 nozzles placed around a central air nozzle. The operating power is equal to 10 kW. The simulations were performed using the commercial code Ansys Fluent with the k-ε realizable model for turbulence closure and the eddy dissipation concept for combustion modelling. The reaction mechanism comprises 19 species and 84 chemical reactions. A post-processing model for the prediction of NO has been used, taking into account the thermal, prompt and N_2O routes for NO formation. The effect of the excess air ratio and inlet air velocity on the temperature and mole fractions of CO, CO_2, O_2 and NO was studied. The influence of the air preheating temperature on the NO molar fraction was also investigated. The predictions are compared with comprehensive experimental data reported in the literature. It is shown that, in general, the model is able to provide good predictions, except in the vicinity of the burner where some discrepancies have been found, which is consistent with past work. The contribution of the prompt mechanism for the formation of NO is negligible, while that of the N_2O route is dominant for all cases investigated, even though the thermal mechanism becomes more important when the air preheating temperature increases.

Keywords: flameless oxidation, laboratory combustor, eddy dissipation concept, pollutant emissions

RESUMO

Neste estudo é apresentada a simulação numérica de uma pequena câmara de combustão cilíndrica operando no regime de combustão sem chama visível. O combustível (metano) é fornecido à câmara através de 15 injectores colocados em torno de um injector central de ar. A potência é igual a 10 kW. As simulações foram efectuadas usando o programa comercial Ansys-Fluent com o modelo de turbulência k-ε realizável e o modelo de combustão EDC - eddy dissipation concept. O mecanismo de reacção é constituído por 19 espécies e 84 reacções químicas. Foi também usado um modelo de pós-processamento para a previsão da fracção molar de NO. A influência do excesso de ar, da velocidade de entrada do ar e da respective temperatura de pré-aquecimento na temperatura e nas fracções molares de CO, CO_2 O_2 e NO foi estudada. As previsões foram comparadas com dados experimentais detalhados disponíveis na literatura. Os resultados mostram que, em geral, o modelo conduz a boas previsões, excepto na vizinhança do queimador, onde foram encontradas algumas discrepâncias sistemáticas, o que é consistente com trabalho anterior. A contribuição do mecanismo rápido para a formação de NO é desprezável, enquanto o mecanismo que tem o N_2O como espécie intermédia é o mais importante em todos os casos analisados, ao passo que a contribuição do mecanismo térmico aumenta à medida que a temperatura de pré-aquecimento do ar aumenta.

Palavras: flameless oxidation, laboratory combustor, eddy dissipation concept, pollutant emissions

ACKNOWLEDGEMENTS

First of all, I would like to thank my advisor Prof. Pedro Jorge Martins Coelho for giving great support during this dissertation. He continuously helped me to increase my knowledge and guided me to find my future aspirations. Moreover, I am grateful to him for recommending me to other universities for Ph.D. related to this study.

I am also grateful to Prof. Krzysztof Pikoń, Prof. Fátima G. da Costa Montemor and Prof. José Alberto Caiado Falcão de Campos for their contributions and continuous efforts to help me finish this study. Furthermore, I also would like to show my gratitude to José Branco and Hildebrando Cruz for advising me to use the tools of the study more efficiently. Also, I would like to express my appreciation to CFD engineer Serkan Duyar who taught me a great deal during my dissertation.

Last but not least, I would like to offer my sincerest gratitude to my family for supporting me throughout this study.

TABLE OF CONTENTS

LIST OF FIGURES

LIST OF TABLES

NOMENCLATURE

Latin Symbols

Small Letters

$a_{\in,i}$ – Emissivity weighting factor for the ith fictitious grey gas

$b_{\in,i,j}$ – Emissivity gas temperature polynomial coefficients

c_i – Concentration

$\bar{c}_{fu}$ – Local mean concentration of fuel

$\bar{c}_{O_2}$ – Local mean concentration of oxidizer

$\bar{c}_{pr}$ – Local mean concentrations of the products

$\bar{c}_{min}$ - The smallest of $\bar{c}_{fu}$ and $\bar{c}_{O_2}/r_{fu}$

e_s – Sensible energy

$\bar{f}$ – Mean component

f' - Fluctuating component

k – Turbulence kinetic energy

m – Non-dimensional value

$\dot{m}$ – Mass flow rate

$\hat{n}$ – Unit surface normal

p – Static pressure

p – Sum of partial pressures of all absorbing gases

r – Radial coordinate

r_w – Point of the wall where boundary condition is applied

r_{fu} – Stoichiometric oxygen requirement to burn 1 kg fuel

q_i – Energy flux

s – Mass stoichiometric ratio

s – Path length

$\hat{s}_i$ – The unit vector in direction i

t – time

u_i – Velocity component in direction i

u_j – Velocity component in direction j

u' - Turbulence velocity

w_j – Quadrature weights

w' - Vorticity

x_i – Position coefficient in direction i

x_j – Position coefficient in direction j

Capital Letters

A_0 – Realizable $k-\varepsilon$ model constant

A_S – Realizable $k-\varepsilon$ model constant

C_p – Heat capacity

$C_{1\varepsilon}$ – Realizable $k-\varepsilon$ model constant

C_2 – Realizable $k-\varepsilon$ model constant

$D_{air\ nozzle}$ – Air inlet nozzle diameter

D_k – Molecular diffusivity

E – Total non-chemical energy

G – Incident radiation

G_k – Generation of turbulence kinetic energy due to the mean velocity gradients

H – Irradiation onto a surface

H – Enthalpy

I – Intensity of radiation

I_b – Blackbody intensity

K_v – Recirculation rate

L' - Length scale

Le – Lewis number

$\dot{M}_A$ – Air mass flow rate

$\dot{M}_E$ – Recirculated exhaust gas mass flow rate

$\dot{M}_F$ – Fuel mass flow rate

P_{fuel} – Operating power

Q – Single step reaction rate

$\dot{Q}$ – Heat source term

R_i – Mean rate of mass transfer between a certain fraction of the fine structures and the surrounding fluid

S_{ij} – Average velocity strain rate

T_F^0 – Temperature of fuel at reference state

T_O^0 – Temperature of oxidizer at reference state

$\overline{T}$ – Local time mean temperature

T_{air} – Air inlet temperature

V_{fuel} – Fuel inlet velocity

V_{air} – Air inlet velocity

V_k – Diffusion velocity

$V_{k,i}$ - i- component of the diffusion velocity V_k of species k

W_F – Molecular weight of fuel

W_O – Molecular weight of oxidizer

X – The fraction of fine structures reacting

Y_F^0 – Mass fraction of fuel at reference state

Y_O^0 – Mass fraction of oxidizer at reference state

Y_O – Mass fraction of oxidizer

Y_F – Mass fraction of fuel

Abbreviations

CDC – Colourless Distributed Combustion

CFD – Computational Fluid Dynamics

C-PDF – Joint Composition Probability Density Function

DNS – Direct Numerical Simulations

DO – Discrete Ordinates Model

EDC – Eddy Dissipation Concept

EDM – Eddy Dissipation Model

EBU – Eddy Break-Up Model

FLOX – Flameless Oxidation

HiTAC – High Temperature Air Combustion

LES – Large Eddy Simulations

LPG – Liquefied Petroleum Gas

MILD – Moderate or Intense Dilution

N – Number of species in the reacting mixture

NO – Nitrogen oxide

NO_x – Nitrogen Oxides

OH* - Hydroxyl radical chemiluminescence

RANS – Reynolds Averaged Navier Stokes

T - Temperature

Greek Symbols

α – Absorptivity

β – Extinction coefficient

γ_λ – Mass fraction of nearly constant energy regions

δ_{ij} – Kronecker symbol

ΔH_R – The heat of reaction

$\Delta h^\circ_{f,k}$ - Formation enthalpy at reference temperature T_0

ε – Turbulence dissipation rate

$\in$ - Emissivity

ϵ_{ijk} – Alternate pseudo tensor

κ – Absorption coefficient

λ – Excess air coefficient

λ – Thermal conductivity

μ – Dynamic viscosity

ρ – Density

ρ – Reflectivity

σ_ε – Turbulent Prandtl number for ε

σ_{ij} – Combination of viscous and pressure tensor in direction i and j

σ_k – Turbulent Prandtl number for k

σ_s – Scattering coefficient

τ_{ij} – Viscous tensor in direction i and j

v'_F – Fuel stoichiometric coefficient

v'_O – Oxidizer stoichiometric coefficient

φ – Scattering phase function

ω_k – Angular velocity

$\dot{w}_k$ – Reaction rate of species k

$\dot{w}_T$ – Heat release due to combustion

Ω – Solid angle

$\bar{\Omega}_{ij}$ - Mean rotation rate viewed in a rotating reference frame with the angular velocity ω_k

Exponents

$(\bar{\ })$ - Reynolds time average

$(\tilde{\ })$ - Favre mass-weighted average

$(\ )'$ - Reynolds fluctuation

$(\ )''$ - Favre fluctuation

$(\ )^o$ – Relative to the fine structure surroundings

$(\ )^*$ - Relative to the fine structures

1. INTRODUCTION

1.1. Scope of the Thesis

Energy demand is increasing dramatically due to population growth and technological advancements over a century. It is apparent that the demand in the energy sector affects economics, politics and environment significantly. In spite of the fact that the energy production from renewable sources such as solar, wind and geothermal has promising future, the role of combustion processes is still very important in energy production processes. Fossil fuels have a share of 82 per cent in world primary energy supply in 2012 and majority of the energy supply is achieved by combustion processes [1].

The environmental effects of using fossil fuels have been becoming a major concern due to high noxious substance emissions since 1970s [2]. Especially, non-efficient coal combustion systems increased the emissions of pollutants due to high sulphur content and high carbon number. Moreover, CO, NO_x and particulate matter emissions from combustion of petroleum products were high in those years. With the improvements in the design of the combustion processes, the emissions decreased significantly. On the other hand, natural gas and methane appear to be a cleaner than other fossil fuels. Especially methane has only one carbon and four hydrogen atoms in the molecules unlike coal or petroleum products. It does not contain sulphur and it has very low NO_x emission as compared to other fossil fuels. Therefore, novel combustion processes have been designed to have lower impact on environment, economy and social lives.

A novel combustion process in 1990s has emerged as a low emission combustion technology which is called flameless oxidation (FLOX) [3]. The reason why it is called flameless oxidation is that there is no visible flame during the combustion process. However, there is always a flame in a combustion process, it can be visible or not. Because of that, some of the scholars chose to give a different name to this combustion technology such as moderate or intense low oxygen dilution (MILD) combustion, high temperature air combustion (HiTAC) or colourless distributed combustion (CDC). This technology is achieved by dilution of reactants with recirculated combustion products. By applying these conditions, more uniform conditions are attained in a combustion chamber. Especially temperature profiles do not have large peaks which lead to very low thermal NO_x emissions. The details of the phenomenon will be described in the ‘’State of the Art’’ chapter.

The majority of combustion processes in the industry are large scale processes. Therefore, it is not very feasible to perform experiments that cover every combination of operating conditions due to physical, economical and time limitations. Instead, simulation software packages have been designed to predict the behaviour of the processes with the advancement of computer technology. In these software packages,

numerical methods are used to predict the solution of the equations that describe the physical phenomena taking place during the combustion process using iterative methods. However, simulation processes can also have economical and time limitations depending on the cases. For that reason the prediction methods used in the software packages also affect the cost and time of computations.

Since FLOX is a novel and promising technology, the research has been done comprehensively both experimentally and numerically. However, more research is needed to understand fully the mechanisms and restrictions of the phenomenon. Therefore, numerical simulations of FLOX cases are a vital part of the research in low emission combustion technologies.

1.2. Objectives

There are two main objectives of this study. One of them is to predict the temperature profiles and species concentrations of four cases for a mild laboratory scale combustor and compare with the experimental data. This analysis is done by using the commercial code Ansys Fluent. The second main goal is to observe the influence of operating conditions in the predictions and how they are matching with the experimental data. Besides the main goals, it is expected to see the effect of grid size in the predictions. Furthermore, different NO models are selected for the NO formation mechanisms in order to assess their influence and to select those that increase the accuracy of the predictions.

1.3. Structure of the Thesis

The thesis contains five chapters. In the first chapter, brief background information about the flameless oxidation is given and the objectives of the study are explained. State of the Art chapter mainly focuses on the theoretical information and previous studies done in relevant topics. In Methods chapter, the techniques used in the simulation tool are described. Moreover, the models used in the simulations and the governing equations are presented. In the fourth chapter, the results obtained from numerous simulations are shown and discussed by comparing with the experimental data. The final chapter gives a closure to the study by summarizing the outcomes of the study.

2. STATE OF THE ART

In this chapter, a literature review of related topics is carried out in order to provide a perspective on current understanding of FLOX. First of all, brief theoretical background is given in combustion types, Eddy Dissipation Concept (EDC) and Flameless Oxidation. Subsequently, previous studies of FLOX cases are explained.

2.1. Combustion Types

There are three types of homogeneous combustion reaction systems in terms of mixing of the fuel and the oxidizer. Premixed combustion occurs when the fuel and oxidizer are mixed prior to ignition whereas partially premixed combustion takes place in reacting systems with both non-premixed and pre-mixed oxidizer/fuel streams [4]. In non-premixed combustion, the fuel and the oxidizer are fed separately to the combustion chamber, and combustion takes place as they mix in the chamber. More details will be given to turbulent non-premixed combustion.

2.1.1. Turbulent Non-Premixed Combustion

Turbulent non-premixed combustion systems are widely used in the industry because the burners are easier to design if compared with the premixed combustion. Moreover, non-premixed combustions systems are safer and more stable than premixed combustion systems since they do not exhibit propagation speed and they do not auto ignite in undesired locations.

There are some processes which make turbulent non-premixed combustion harder to understand and design than turbulent premixed combustion. In turbulent non-premixed combustion, the molecules reach the flame front before reacting by molecular diffusion. Therefore, non-premixed flames are called diffusion flames. During this transport of molecules, the diffusion of the species generally limits the overall reaction rate. Because of that, chemical reactions are often assumed to be very fast or infinitely fast in many combustion models.

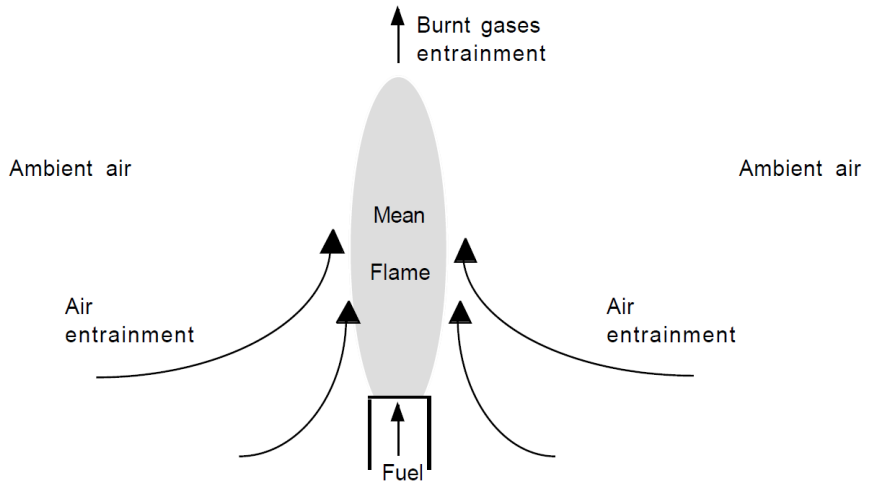

Figure 1. Turbulent non-premixed flame

Reacting species are entrained by oxidizer to the mean flame zone as shown in Figure 1 [5]. One of the most challenging design criteria is flame stabilization. If the stabilization is not enough, it may lead an unsafe operation of a combustion chamber especially at high powers.

2.2. Eddy Dissipation Concept (EDC)

For Reynolds Averaged Navier Stokes (RANS) simulations, combustion and turbulence models are required to perform CFD calculations. For instance, k-epsilon or k-omega models can be used for turbulence whereas EDC or Joint Composition Probability Density Function (C-PDF) can be used for combustion. These combustion models establish the connection between turbulence and chemistry. A brief explanation will be given to EDC which is the model used in the thesis.

Eddy Dissipation Concept is basically an upgraded version of Eddy Dissipation Model (EDM) which allows more detailed chemical mechanisms [5]. In this model, the fuel mean burning rate is calculated by using fuel, oxidizer and combustion products mean mass fractions. It describes the concept of turbulent energy transfer in Figure 2 [6].

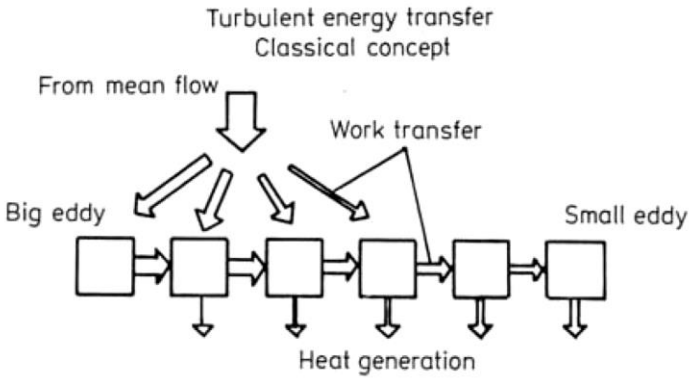

Figure 2. Turbulent energy transfer

In a turbulent flow, different sizes of eddies are observed. First of all, the energy from mean flow is distributed to big eddies [6].Then, the work transfer between big eddies and smaller eddies occurs. Because of the interactions between the main flow and big eddies, kinetic energy is produced. Then the kinetic energy is converted to heat due to the contacts of eddies between them. The heat is generated mostly in the smallest eddies In a turbulent flow, chemical reactions depend highly on the molecular mixing [7]. These micro scale molecular mixing processes occur in very small regions of the entire volume of the fluid. In those small regions, there are fine structures whose dimensions are small in one or two

directions, not in the third, which is shown in Figure 3. The conversion of turbulence into heat takes place in these fine structures. According to the model developed by Magnussen, 3/4 of the dissipation of energy into heat takes place at the fine structure level [8].

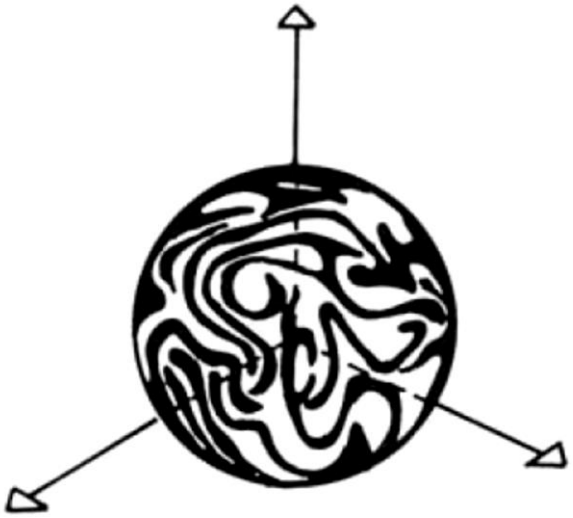

Figure 3. Schematic illustration of fine structures developed on a constant energy surface

2.3. Flameless Combustion

2.3.1. Fundamentals

In traditional combustion systems, a visible flame is created by the mixture of the fuel and oxidizer supplied. If the mixing in a combustion chamber is not sufficient, there might be high local temperatures and high gradient of species concentrations. Especially, very high local temperatures may increase the formation of thermal NO significantly. Basically, the uniformity in the chamber is violated by these issues. In order to prevent this non-uniformity, a new combustion mode has been developed nearly two decades ago. This new combustion mode is achieved by pre-heated air and high flue gas recirculation. By means of these modifications applied to combustion processes, no visible flame occurs and the reactions are distributed to a larger volume. Verissimo et. al suggested that ‘’Under flameless oxidation conditions combustion takes place in a distributed reaction zone rather than in a thin flame front, with relatively uniform and low temperatures and temperature fluctuations, in comparison to conventional flames’’ [9]. Moreover, it must be stated that in flameless oxidation, the temperature of the reactants must be higher than the auto-ignition temperature of fuel-oxidizer mixture.

This new technology has been investigated also for large scale industry applications such as gas turbine combustors. Li et al. investigates the application of flameless combustion to a gas turbine combustor [10]. They found that at specific air pre-heat temperatures, air flow rates and specific values of excess air ratio (λ), flameless mode is achieved with extremely low pollutant concentrations.

Figure 4 shows the temperature profiles of three different combustion processes [3]. In the first two processes, temperature fluctuations in combustor are rather high compared to HiTAC (same as FLOX). The more heat extracted from flue gases, more uniform temperature is obtained. Moreover, it can be

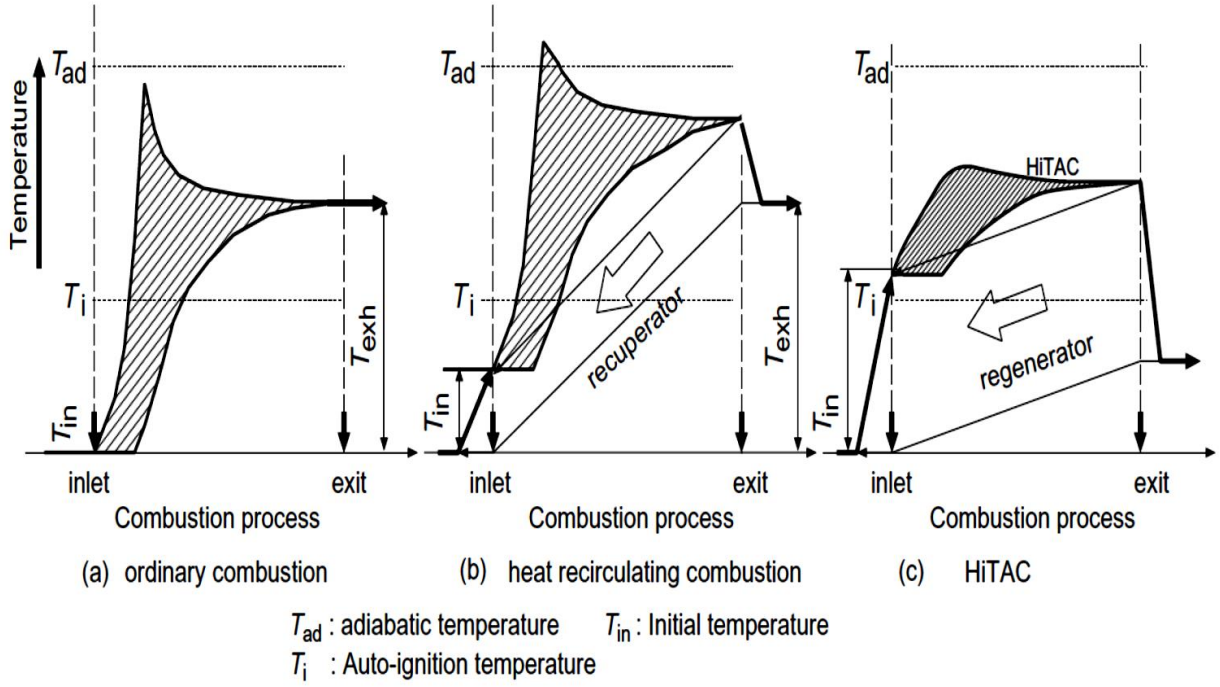

Figure 4. Conceptual temperature histories and fluctuation density

seen in HiTAC that the peak temperature is quite lower as compared to the other two systems.

In a study carried out by Li et al. [10], main characteristics of mild combustion are described as;

- High entrainment of air and fuel supplied to the system and high pre-heating of combustion air,
- Adequate recirculation of hot flue gases to dilute the fuel and air mixture by inert gases,
- Maintaining the temperature higher than auto ignition temperature of the mixture and establishment of less than 5-10 % local oxygen concentration

Moreover, Tsuji et al. [3] suggested that by applying the conditions above the thermal efficiency of the combustion process can be increased by 30 %. In terms of NO_x reduction, less than 1/3 of emission of conventional low NO_x burners can be achieved [3].

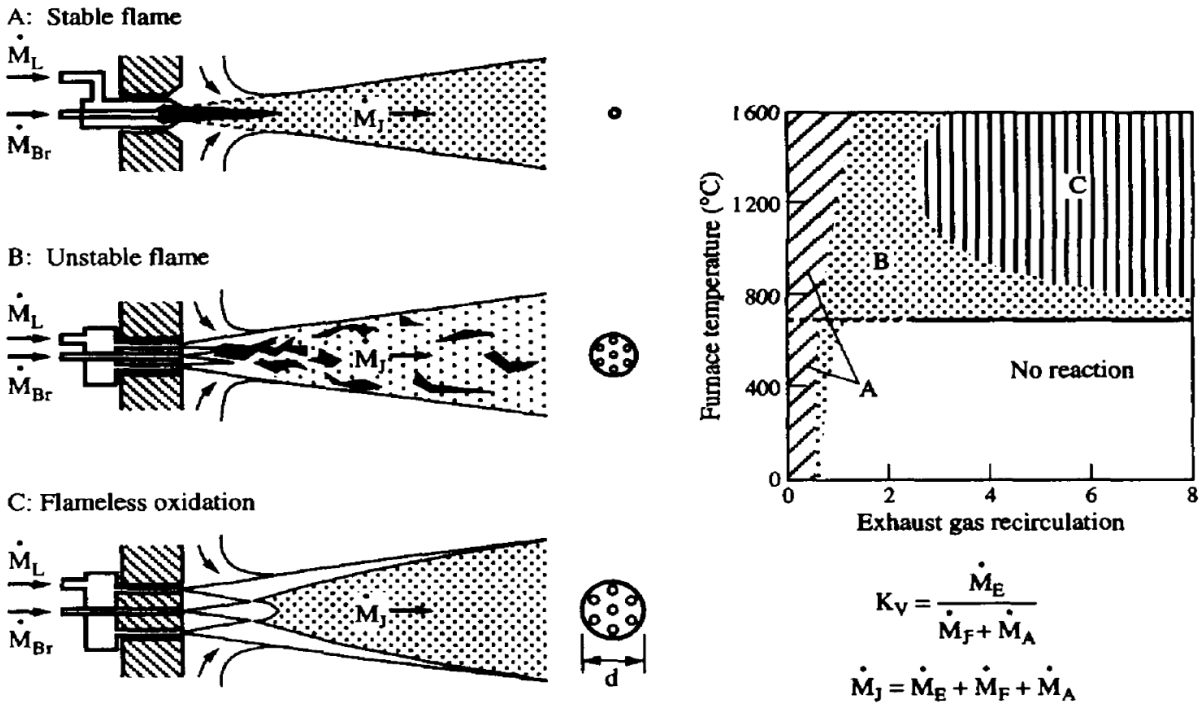

Figure 5. Stability limits

Figure 5 shows a comparison of the flames of different combustion modes and exhaust gas recirculation rates [11]. Exhaust gas recirculation is defined as follows:

$$K_v = \frac{\dot{M}_E}{\dot{M}_F + \dot{M}_A} \tag{1}$$

where K_v is the recirculation rate, $\dot{M}_E$ is recirculated exhaust gas mass flow rate, $\dot{M}_F$ is fuel mass flow rate and $\dot{M}_A$ is air mass flow rate.

It is possible to have a stable flame 'A' at even very low or very high temperatures. However, when the recirculation rate is increased, the flame becomes unstable 'B' and it will lead to inefficient combustion. If exhaust gas recirculation and furnace temperature is sufficiently high, it is possible to achieve a stable flameless oxidation 'C'. Minimum recirculation rate K_v is around 2.5 for obtaining flameless oxidation [11].

On the other hand, it is clear that the temperature field in a combustor might have a big effect on nitric oxides production [12]. Especially thermal NO mechanism appears as the dominating mechanism of NO_x formation at elevated temperatures [13]. Furthermore, air pre-heat temperature has also a significant role in NO_x formation which is illustrated in Figure 6 [3].

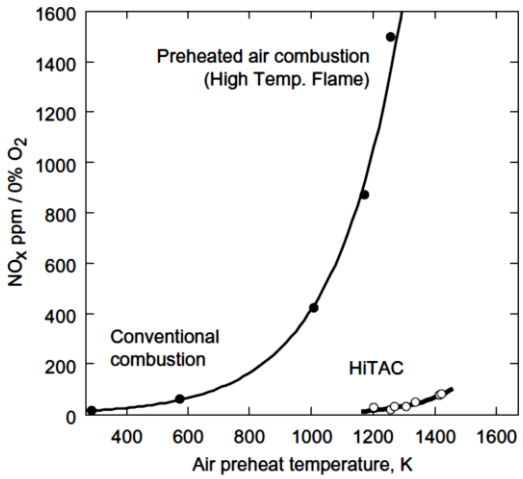

Figure 6. Effect of air pre-heat temperature on NO_x formation

Particularly in conventional combustion, an increase of air pre-heat temperature causes NO_x emissions to increase exponentially. However, there is a major decrease in NO_x emissions when HiTAC technology is used even at very high air pre-heat temperatures.

2.3.2. Numerical Simulation of FLOX

Numerical simulation of reacting turbulent flows is achieved by three different computational approaches [5]. FLOX CFD simulations are also carried out using the same approaches:

- Reynolds Averaged Navier Stokes (RANS) is the first computational approach to compute the turbulent flow. However, since the prediction of instantaneous flow field in a turbulent flame was not possible, RANS equations are derived to solve the mean values of all quantities. The averaged equations obtained from Reynolds or Favre, are not enough to close the system. Therefore, a turbulence model is needed to solve RANS equations such as k-ε model.
- Large Eddy Simulations (LES) are the second approach to predict the turbulent flow. In this computational method, large scale eddies are explicitly solved whereas small scale eddies are modeled using sub-grid models. In other words, LES is able to calculate instantaneous large scales but sub-grid models are needed to take into account the small scales.

- The last approach of the computational methods is Direct Numerical Simulations (DNS). By using DNS simulations all turbulence scales can be solved explicitly unlike RANS. Moreover, it differs from LES in the sense that DNS is able to solve even the smallest turbulent scales without the need of sub-grid models.

In Table 1, the comparison between the three approaches of numerical simulation of turbulent combustion is shown [5]. Each method has advantages and disadvantages. For instance, RANS has reduced numerical costs while models are required for the simulations. On the other hand, DNS does not need any model whereas it has prohibitive computational costs.

Table 1. Comparison between RANS, LES and DNS approaches for numerical simulations of turbulent combustion

Approach	**Advantages**	**Drawbacks**
RANS	- ''Coarse'' numerical grid - Geometrical simplification (2D flows, symmetry,…) - ''Reduced'' numerical costs	- Only mean and converged flow fields are resolved - Models required
LES	- Unsteady features - Reduced modeling impact (compared to RANS)	- Models required - Unsteady simulations required - Needs accurate numerical scheme - Computational costs
DNS	- No models needed for turbulence closure - Tool to study models	- Prohibitive numerical costs (fine grids, accurate numerical scheme - Limited to academic problems

DNS is the most demanding method among all and it is limited to only academic scale such as combustion in a small box. LES allows coarser grids than DNS and it can work with relatively high Reynolds number. However, sub-grid scale models are needed. On the other hand, RANS is the most common method used in CFD applications due to its practicality and low numerical costs. However, the validity of the results depends on the turbulence and combustion models defined.

2.4. Previous Studies

In this section, previous studies related with FLOX will be overviewed. The papers reviewed here are both experimental and numerical cases. Some of the cases presented here use the same case and geometry but different operating conditions such as excess air ratio or air inlet velocity.

Characteristics of the reactions zone in a combustor operating at mild combustion is investigated by Özdemir et al [14]. They discovered that the hydroxyl radical chemiluminescence (OH*) is distributed more uniformly along the combustion chamber in MILD operating conditions unlike conventional combustion.

Orsino et. al carried out numerical simulations of combustion of natural gas with high-temperature air, pre-heated to 1300 ^{o}C. They tested three combustion models, namely Eddy Break-Up model (EBU), Eddy Dissipation Concept (EDC) and PDF/Mixture Fraction model [15]. According to the results, all of the numerical models yielded low NO_x and CO emissions and uniform profiles of combustion chamber. EDC and PDF models gave identical good predictions of NO formation except a small region in natural gas jet.

Numerical and experimental investigation of a mild combustion burner was done by Galletti et al [16]. They observed higher burner efficiency in terms of thermal efficiency in MILD conditions. It was also analyzed in this study that in MILD combustion, the high temperature region was characterized by Damköhler number lower than conventional combustion.

Szegö et al. examined the operational characteristics of a parallel jet mild combustion burner system. They investigated natural gas and LPG combustion with increasing N_2 and CO_2 dilution [17]. When the natural gas/N_2 is 50/50 by mass no visible flame was observed. In the case of LPG, the requirement of inert CO_2 was more than N_2 and double of LPG by mass to achieve flameless conditions. Moreover, they recorded 14 ppm dry NO_x at 3 % O_2 where the equivalence ratio was 0.9.

For gas turbine applications there are some studies to obtain a flameless combustion regime in the gas turbine combustor. Guillou et al. investigated the application of flameless combustion for gas turbine engines [18]. In order to obtain the desired conditions, the equivalence ratio was decreased approximately to 0.35-0.4 region. However, when the equivalence ratio decreased, the exit temperature from the combustor also decreased. Therefore, it became very hard to obtain a flameless combustion even with infinite gas recirculation where 800 ^{o}C of initial temperature is required in the combustor. Thus, high exit temperature from compressor is required. It was suggested that with the current compressor technologies, it is unlikely to achieve that required compressor discharge.

Additionally, M. Castela et al. studied the effect of air inlet temperatures at different excess air coefficients on mean (OH*) images using a reverse flow reactor [19].

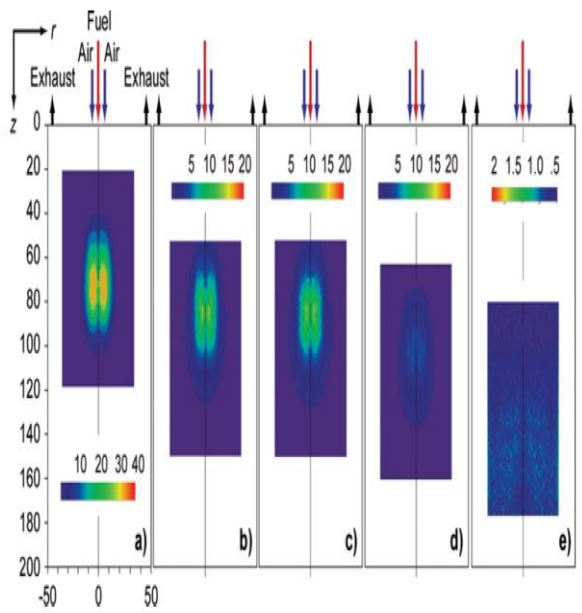

Figure 8. Mean OH* images as a function of excess air coefficient for an air inlet temperature of 325 ^{o}C. (a) λ = 1.3, (b) λ = 1.5, (c) λ = 1.6, (d) λ = 2, (e) λ = 2.4

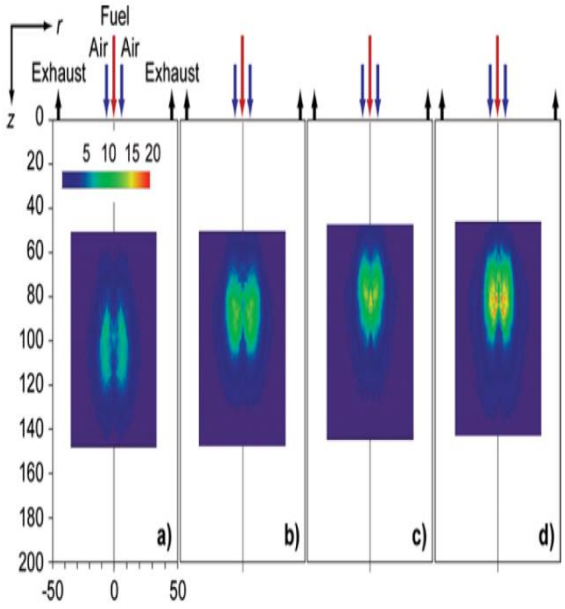

Figure 8. Mean OH* images as a function of the air inlet temperature for an excess air coefficient of 1.4. (a) 25 ^{o}C, (b) 225 ^{o}C, (c) 425 ^{o}C, (d) 525 ^{o}C

They found that the intensity of OH* images starts to disappear as λ increases. Especially for λ greater than 1.6, OH* starts to be distributed volumetrically which leads more uniform combustion chamber and less temperature and species concentration gradients. Moreover, they observed that OH* intensities increase and gets concentrated nearby the burner with the increase of air inlet temperature.

Numerical investigation of a small scale combustor study was done by Coelho et al. [20]. The numerical investigation is done by commercial code Fluent with semi-detailed mechanism. In the study, two different combustion models, namely EDC and C-PDF were used to predict the temperature field and the gradients of species concentrations. They found some discrepancies of temperature and CO molar fraction in the vicinity of the burner especially when Eddy Dissipation Concept (EDC) was used. Temperature profiles and species concentrations are shown in Figure 9 [20].

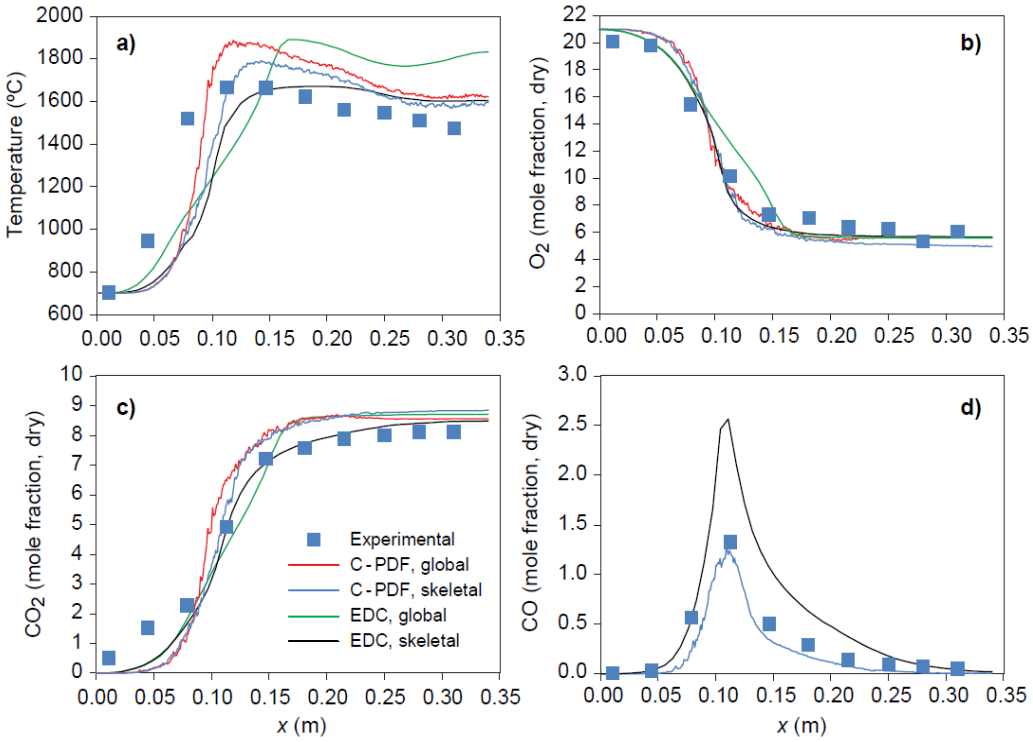

Figure 9. Predicted and measured axial profiles of mean temperature, O_2, CO_2 and CO molar fractions on a dry basis

Costa et al. investigated the importance of the inlet air velocity on the establishment of flameless combustion in a laboratory combustor [9]. They achieved different air inlet velocities by changing the size of the air nozzle. In this study, it was observed that as V_{air} increases at constant excess air ratio λ =1.3, the reaction zone did not move whereas the intensities of OH* decreased which happens in flameless oxidation conditions. They could not observe a flameless combustion if λ was greater than 1.7 independent of the air inlet velocity. Furthermore, Costa et al. also studied influence of the thermal input on the reaction zone under flameless oxidation conditions experimentally [21]. The fuel (methane) thermal input was varied between 7 kW and 13 kW. They maintained the excess air ratio values low enough to keep the flameless regime. As the thermal input increased, the reaction zone intensity increased while it was moving towards exhaust. NO_x emissions did not vary considerably while changing the thermal input. However, CO emissions increased when the thermal input increased.

3. METHODS

3.1. Introduction

In this chapter, the modeling aspects of the phenomena used in the study of the thesis are described. First of all, the equations describing conservation equations for reacting flows are given. Then, RANS equations are described. Moreover, the equations concerning the turbulence model, combustion model and radiation model used in the study are designated. Additionally, the modeling characteristics of NO are explained including the three mechanisms of NO. Finally, the computational details used in the commercial code ANSYS Fluent are explained such as grid details and solution methods.

3.2. Conservation Equations for Reacting Flows

The first step of modeling approach is the description of main conservations equations for reacting flows and their assumptions. Firstly, conservation of momentum, afterwards conservation of mass and species and finally conservation of energy are described [5].

Conservation of momentum is the same for both reacting and non-reacting flows. The following equation designates the conservation of momentum:

$$\frac{\partial}{\partial t}\rho u_j + \frac{\partial}{\partial x_i}\rho u_i u_j = -\frac{\partial p}{\partial x_j} + \frac{\partial \tau_{ij}}{\partial x_i} = \frac{\partial \sigma_{ij}}{\partial x_i} \tag{2}$$

where t is time, x_i and x_j are the cartesian coordinates in direction i and j, ρ is density, p is the static pressure, u_i and u_j are the velocity components in directions i and j. τ_{ij} is the viscous tensor in direction i and j, σ_{ij} is representing the combination of viscous and pressure tensor in direction i and j.

$$\tau_{ij} = -\frac{2}{3}\mu\frac{\partial u_k}{\partial x_k}\delta_{ij} + \mu\left(\frac{\partial u_i}{\partial x_j} + \frac{\partial u_j}{\partial x_i}\right) \tag{3}$$

$$\text{and} \qquad \sigma_{ij} = \tau_{ij} - p\delta_{ij} \tag{4}$$

where μ is the dynamic viscosity and δ_{ij} is the Kronecker symbol: $\delta_{ij} = 1$ if i = j, 0 otherwise.

Similarly conservation of mass is also the same for both non-reacting and reacting flows which is represented in the equation below:

$$\frac{\partial \rho}{\partial t} + \frac{\partial \rho u_i}{\partial x_i} = 0 \tag{5}$$

For species k;

$$\frac{\partial \rho Y_k}{\partial t} + \frac{\partial}{\partial x_i}\left(\rho\left(u_i + V_{k,i}\right)Y_k\right) = \dot{w}_k \qquad for\ k = 1 \ldots, N \tag{6}$$

where $V_{k,i}$ is the i- component of the diffusion velocity V_k of species k, Y_k is the mass fraction, $\dot{w}_k$ is the reaction rate of species k and N is the number of species in the reacting mixture.

Conservation of energy is different than the non-reacting flow, because there is combustion taking place and it contributes to the energy equation. The energy conservation equation based on the summation of sensible and kinetic energies is represented in the equation below:

$$\frac{\partial \rho E}{\partial t} + \frac{\partial}{\partial x_i}(\rho u_i E) = \dot{w}_T - \frac{\partial q_i}{\partial x_i} + \frac{\partial}{\partial x_j}\left(\sigma_{ij} u_i\right) + \dot{Q} \tag{7}$$

where E is the total non-chemical energy, $\dot{w}_T$ is the heat release due to combustion, q_i is the energy flux, $\dot{Q}$ is the heat source term (for instance electric spark, a laser or a radiative flux). Expanded forms of these variables can be found in the equations 8-10:

$$E = H - \frac{p}{\rho} = e_s + \frac{1}{2} u_i u_i \tag{8}$$

Where H is the enthalpy term and e_s is the sensible energy.

$$\dot{w}_T = -\sum_{k=1}^{N} \Delta h^\circ_{f,k}\, \dot{w}_k \tag{9}$$

where $\Delta h^\circ_{f,k}$ is the formation enthalpy at reference temperature T_0.

$$q_i = -\lambda \frac{\partial T}{\partial x_i} + \rho \sum_{k=1}^{N} h_k Y_k V_{k,i} \tag{10}$$

where λ is the thermal conductivity and T is the temperature and h_k is the sensible enthalpy of species k.

Generally, the complete form of energy equation is not needed for most of the deflagration cases where pressure is constant, body forces are zero and viscous heating is insignificant. For the constant pressure, low Mach number flames the energy equation can be simplified to equation 11:

$$\frac{\partial \rho E}{\partial t} + \frac{\partial}{\partial x_i}(\rho u_i E) = \dot{w}_T - \frac{\partial q_i}{\partial x_i} \tag{11}$$

3.3. RANS Equations of Turbulent Non-Premixed Combustion

RANS is based on the elimination of the unsteadiness by averaging out the instantaneous Navier-Stokes equations [22]. In this method, all of the turbulence scales are modeled and only the mean flow is resolved. In a constant density flow, Reynolds averaging splits any parameter into a mean $\bar{f}$ and a fluctuating f' component ($f = \bar{f} + f'$). This procedure is first applied to conservation of mass equation:

$$\frac{\partial \bar{\rho}}{\partial t} + \frac{\partial}{\partial x_i}(\overline{\rho u_\iota}) = \frac{\partial \bar{\rho}}{\partial t} + \frac{\partial}{\partial x_i}(\bar{\rho}\bar{u}_\iota + \overline{\rho' u_\iota'}) = 0 \;\; or \;\; \frac{\partial \bar{\rho}}{\partial t} + \frac{\partial}{\partial x_i}(\bar{\rho}\bar{u}_\iota) = -\frac{\partial}{\partial x_i}(\overline{\rho' u_\iota'}) \tag{12}$$

where $\overline{\rho' u_\iota'}$ corresponds to the correlation between density and velocity fluctuations and requires modeling. If the density is variable, Reynolds averaging creates more unclosed correlations between any quantity f and density fluctuations. In order to overcome this, mass-weighted averages which are called Favre averages are introduced:

$$\widetilde{f} = \frac{\overline{\rho f}}{\bar{\rho}} \tag{13}$$

$$f = \widetilde{f} + f'' \quad \text{with} \quad \widetilde{f''} = 0 \tag{17}$$

After all, the modification of the conservation equations is applied;

- For conservation of mass;

$$\frac{\partial \bar{\rho}}{\partial t} + \frac{\partial}{\partial x_i}(\bar{\rho}\widetilde{u_\iota}) = 0 \tag{18}$$

- For conservation of momentum;

$$\frac{\partial \bar{\rho}\widetilde{u_\iota}}{\partial t} + \frac{\partial}{\partial x_i}\left(\bar{\rho}\widetilde{u_\iota}\widetilde{u_j}\right) + \frac{\partial \bar{p}}{\partial x_j} = \frac{\partial}{\partial x_i}\left(\bar{\tau}_{ij} - \bar{\rho}\widetilde{u_\iota'' u_j''}\right) \tag{19}$$

- For conservation of chemical species;

$$\frac{\partial \bar{\rho}\tilde{Y}_k}{\partial t} + \frac{\partial}{\partial x_i}\left(\bar{\rho}\widetilde{u_\iota}\tilde{Y}_k\right) = -\frac{\partial}{\partial x_i}\left(\overline{V_{k,\iota}Y_k} + \bar{\rho}\widetilde{u_\iota''Y_k''}\right) + \bar{\dot{w}}_k \qquad for\ k = 1, N \tag{20}$$

- For conservation of enthalpy;

$$\frac{\partial \bar{\rho}\tilde{h}_s}{\partial t} + \frac{\partial}{\partial x_i}\left(\bar{\rho}\widetilde{u_\iota}\tilde{h}_s\right) = \bar{\dot{w}}_T + \frac{\overline{Dp}}{Dt} + \frac{\partial}{\partial x_i}\left(\overline{\lambda\frac{\partial T}{\partial x_\iota}} - \overline{\rho u_\iota'' h_s''}\right) + \overline{\tau_{\iota J}\frac{\partial u_\iota}{\partial x_J}} - \frac{\partial}{\partial x_i}\left(\overline{\rho\sum_{k=1}^{N} V_{k,\iota}Y_k\, h_{s,k}}\right) \tag{21}$$

where

$$\frac{\overline{Dp}}{Dt} = \frac{\partial \bar{p}}{\partial t} + \overline{u_\iota\frac{\partial p}{\partial x_\iota}} = \frac{\partial \bar{p}}{\partial t} + \widetilde{u_\iota}\frac{\partial \bar{p}}{\partial x_i} + \overline{u_\iota''\frac{\partial p}{\partial x_\iota}} \tag{22}$$

The equations above represent the balance equations for general cases without simplifications. However, for turbulent non-premixed flames some assumptions can be made [5]:

- The thermodynamic pressure is constant and Mach numbers are small,
- Species heat capacities are equal and constant ($C_{pk} = C_p$)
- Molecular diffusivities are equal for all species ($D_k = D$)
- Lewis numbers are assumed to be unity. ($Le = \lambda/\rho C_p D = 1$)
- Fuel and oxidizer are supplied to the combustion chamber with reference state (T_F°, Y_F°) for fuel and (T_O°, Y_O°) for oxidizer.

Moreover, mass fractions of fuel and oxidizer are connected through the mixture fraction z under the assumption of single step chemistry in adiabatic flows;

$$z = \frac{sY_F - Y_O + Y_O^0}{sY_F^0 + Y_O^0} = \frac{\frac{C_p}{Q}\left(T - T_O^0\right) + Y_F}{\frac{C_p}{Q}\left(T_F^0 - T_O^0\right) + Y_F^0} = \frac{\frac{sC_p}{Q}\left(T - T_O^0\right) + Y_O - Y_O^0}{\frac{sC_p}{Q}\left(T_F^0 - T_O^0\right) - Y_O^0} \tag{23}$$

In the equation above, Q is the heat of reaction and s is the mass stoichiometric ratio which is $s = \frac{v_O' W_O}{v_F' W_F}$ where v_O' and v_F' are the molar stoichiometric coefficients and W_O and W_F are the molecular weights of the oxidizer and fuel.

The simplifications above lead to some modifications in the conservation of chemical species and conservation equation for mixture fraction;

- New form of conservation of chemical species is;

$$\frac{\partial \bar{\rho}\tilde{Y}_k}{\partial t} + \frac{\partial}{\partial x_i}\left(\bar{\rho}\tilde{u_\iota}\tilde{Y}_k\right) = \frac{\partial}{\partial x_i}\left(\overline{\rho D_k \frac{\partial Y_k}{\partial x_\iota}} - \bar{\rho}\widetilde{u_\iota'' Y_k''}\right) + \bar{\dot{w}}_k \qquad for\ k = 1, N \tag{24}$$

- Conservation equation for mixture fraction is;

$$\frac{\partial \bar{\rho}\tilde{z}}{\partial t} + \frac{\partial}{\partial x_i}\left(\bar{\rho}\tilde{u_\iota}\tilde{z}\right) = \frac{\partial}{\partial x_i}\left(\overline{\rho D \frac{\partial z}{\partial x_\iota}} - \bar{\rho}\widetilde{u_\iota'' z''}\right) \tag{25}$$

The averaged equations include some unclosed terms which are required to be modeled such as turbulent fluxes and reaction terms. Turbulent scalar transport ($\widetilde{u_\iota'' Y_k''}$) and ($\widetilde{u_\iota'' z''}$) are modeled using a gradient assumption [5]. On the other hand, Reynolds stresses ($\widetilde{u_\iota'' u_j''}$) and the reaction term ($\bar{\dot{w}}_k$) need to be closed by using a turbulence model and a reaction model. In the next chapters, the turbulence and reaction models used in the study are explained.

3.4. Turbulence Model: Realizable k-ε Model

The closure of Reynold stresses can be done by several turbulence models. First approximation was done by Boussinesq et al. and it is related with the turbulent dynamic viscosity μ_t [5].

$$\bar{\rho}\widetilde{u_\iota'' u_j''} = -\mu_t\left(\frac{\partial \tilde{u}_i}{\partial x_j} + \frac{\partial \tilde{u}_j}{\partial x_i} - \frac{2}{3}\delta_{ij}\frac{\partial \tilde{u}_k}{\partial x_k}\right) + \frac{2}{3}\bar{\rho}k \tag{26}$$

where δ_{ij} is the Kronecker symbol and k is the turbulence kinetic energy which is described as;

$$k = \frac{1}{2}\sum_{k=1}^{3}\widetilde{u_k'' u_k''} \tag{27}$$

The dynamic viscosity calculation was proposed by Shih et al [23].

$$\mu_t = \rho C_\mu \frac{k^2}{\varepsilon} \tag{28}$$

The formula requires the solutions of k and ε separately. On the other hand, C_μ is a constant in standard and RNG $k-\varepsilon$ models but not in realizable $k-\varepsilon$ model. It is computed from the following expression [24].

$$C_\mu = \frac{1}{A_0 + A_S U^* \frac{k}{\varepsilon}} \tag{29}$$

where A_0 and A_S are model constants, and U^* is expressed as the following [25]:

$$U^* = \sqrt{S_{ij}S_{ij} + \tilde{\Omega}_{ij}\tilde{\Omega}_{ij}} \tag{30}$$

$$\tilde{\Omega}_{ij} = \Omega_{ij} - 2\epsilon_{ijk}\omega_k \tag{31}$$

$$\Omega_{ij} = \bar{\Omega}_{ij} - \epsilon_{ijk}\omega_k \tag{32}$$

where S_{ij} is the average velocity strain rate, and $\bar{\Omega}_{ij}$ is the mean rotation rate viewed in a rotating reference frame with the angular velocity ω_k, and ϵ_{ijk} is the alternate pseudo tensor.

The model constants A_0 and A_S are:

$$A_0 = 4.04 \text{ and } A_S = \sqrt{6}\cos\emptyset$$

where,

$$\emptyset = \frac{1}{3}\cos^{-1}\left(\sqrt{6}W\right), \qquad W = \frac{S_{ij}S_{jk}S_{ki}}{\tilde{S}^3}, \tag{33), (34}$$

$$\tilde{S} = \sqrt{S_{ij}S_{ij}}, \;\; S_{ij} = \frac{1}{2}\left(\frac{\partial u_j}{\partial x_i} + \frac{\partial u_i}{\partial x_j}\right) \tag{35), (36}$$

Two transport equations for turbulence kinetic energy (k) and turbulence dissipation rate (ε) are solved in the Realizable k-ε model where k-equation is similar to standard and RNG models except for the model constants. However, the structure of the dissipation rate equation is different from the others:

$$\frac{\partial}{\partial t}(\rho k) + \frac{\partial}{\partial x_j}(\rho k u_j) = \frac{\partial}{\partial x_j}\left[\left(\mu + \frac{\mu_t}{\sigma_k}\right)\frac{\partial k}{\partial x_j}\right] + G_k - \rho\varepsilon - Y_M \tag{37}$$

and

$$\frac{\partial}{\partial t}(\rho\varepsilon) + \frac{\partial}{\partial x_j}(\rho\varepsilon u_j) = \frac{\partial}{\partial x_j}\left[\left(\mu + \frac{\mu_t}{\sigma_\varepsilon}\right)\frac{\partial \varepsilon}{\partial x_j}\right] + \rho C_{1\varepsilon} S - \rho C_2 \frac{\varepsilon^2}{k + \sqrt{v\varepsilon}} \tag{38}$$

where

$$C_1 = max\left[0.43, \frac{\eta}{\eta + 5}\right], \quad \eta = S\frac{k}{\varepsilon}, \quad S = \sqrt{2S_{ij}S_{ij}} \tag{39}$$

In the transport equations above, G_k is the generation of turbulence kinetic energy due to the mean velocity gradients and it can be calculated as follows:

$$G_k = -\rho\overline{u_i{}' u_j{}'}\frac{\partial u_j}{\partial x_i} \tag{40}$$

σ_k in k-equation represents the turbulent Prandtl number for k and σ_ε in ε-equation represents the turbulent Prandtl number for ε. C_2 and$C_{1\varepsilon}$ are constants. The values of these four terms are given below:

$$\sigma_k = 1, \quad \sigma_\varepsilon = 1.2, \quad C_2 = 1.9, \quad C_{1\varepsilon} = 1.44$$

3.5. Combustion Model: Eddy Dissipation Concept (EDC)

The Eddy Dissipation Concept (EDC) is a model for turbulence/chemistry interaction. The principles of EDC are explained in the State of the Art chapter. In this section, the details of closure of the reaction terms in conservation equations are clarified by EDC. First of all, the modeling of interstructural energy transfer is explained. Subsequently, modeling of the fine structures and molecular mixing process is described. Finally, modeling of the reaction processes is given.

Figure 10 illustrates a modeling scheme for mechanical energy transfer from bigger to smaller turbulence structures [26]:

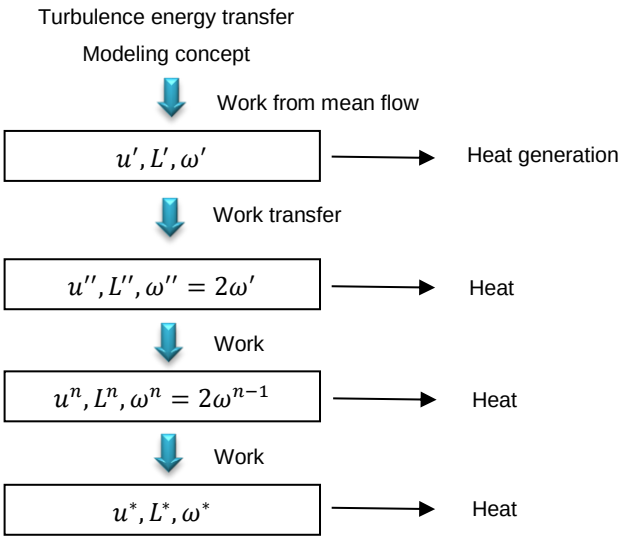

Figure 10. The modeling concept of transfer of mechanical energy

The first structure level is represented by a turbulence velocity, u', a length scale, L', and vorticity or characteristic strain rate:

$$\omega' = \frac{u'}{L'} \tag{41}$$

For the smallest structure level, fine structures, characteristic scales are defined as follows:

$$u^* = 1.74\ (\varepsilon.\nu)^{1/4} \tag{42}$$

$$L^* = 1.43\ \ \nu^{\frac{3}{4}}/\ \varepsilon^{\frac{1}{4}} \tag{43}$$

where u^* is the mass average fine structure velocity, and L^* is the characteristic length scale.

The mass fraction of fine structures can be expressed by:

$$\gamma^* = \left(\frac{u^*}{u'}\right)^3 \tag{44}$$

If the fine structures are assumed to be localized in nearly constant energy regions, then the mass fraction of these regions are:

$$\gamma_\lambda = \frac{u^*}{u'} \;\; and \;\; \gamma^* = \gamma_\lambda * \left(\frac{u^*}{u'}\right)^2 \qquad (45), (46)$$

If isotropic turbulence is assumed and the mass fraction is related with the turbulence kinetic energy and its dissipation rate:

$$\gamma^* = 9.7\left(\frac{v.\varepsilon}{k^2}\right)^{3/4} \quad and \quad \gamma_\lambda = 2.13\left(\frac{v.\varepsilon}{k^2}\right)^{1/4} \qquad (47), (48)$$

Reynolds number is related with the mass fraction in the following way:

$$\gamma^* = 40.2{Re_\lambda}^{-3/2} \;\; and \;\; \gamma_\lambda = 3.42{Re_\lambda}^{-1/2} \qquad (49), (50)$$

If a simple geometry of fine structures is assumed, mass transfer per unit of time and unit of mass of the fluid between the fine structures and the surrounding can be defined as follows:

$$\dot{m} = 2\frac{u^*}{L^*}\,.\gamma^* \qquad (51)$$

If k and ε are included in mass transfer equation it turns into the following form:

$$\dot{m} = 23.6\left(\frac{v.\varepsilon}{k^2}\right)^{1/4}\frac{\varepsilon}{k} \qquad (52)$$

The rate of mixing between the fine structures and the surrounding fluid determines the rate of molecular mixing. The mean rate of mass transfer between a certain fraction of the fine structures and the surrounding fluid R_i can be written as [26}:

$$R_i = \dot{m}\,.X\left(\frac{c_i^o}{\rho^\circ} - \frac{c_i^*}{\rho^*}\right) \qquad (53)$$

where X is the fraction of fine structures reacting and c_i, refers to concentration. ° and * represent the conditions in the surrounding and the fine structures.

The mass transfer rate R_i^*, can also be written per unit volume in the fine structure fraction:

$$R_i^* = \frac{\dot{m}\,.\rho^*}{\gamma^*}\left(\frac{c_i^o}{\rho^\circ} - \frac{c_i^*}{\rho^*}\right) \qquad (54)$$

Lastly, the mean concentration of species i can be expressed as follows:

$$\frac{\bar{c}_i}{\bar{\rho}} = \frac{c_i^*}{\rho^*} \,.\gamma^* \,.X + \frac{c_i^o}{\rho^\circ} \,.(1 - \gamma^* \,.X) \tag{55}$$

In case of infinitely fast reaction rate, mass transfer between the fine structures and surroundings will be limiting the reaction rate. In case of flameless combustion, the concentration of fuel and oxygen in the fine structures will be very small and the reaction rate would be expressed in the following way if the reaction took place in all fine structures:

$$R_{fu} = \dot{m} \,.\frac{\bar{c}_{min}}{1 - \gamma^*} \tag{56}$$

where $\bar{c}_{min}$ is the smallest of $\bar{c}_{fu}$ and $\bar{c}_{O_2}/r_{fu}$, where $\bar{c}_{fu}$ and $\bar{c}_{O_2}$ are the local mean concentrations of fuel and oxygen and r_{fu} is stoichiometric oxygen requirement to burn 1 kg fuel.

However, all of the fine structures may not react due to insufficiency of heat. In that case, the fraction of fine structures which are reacting can be expressed as such:

$$X = \frac{\bar{c}_{pr} / \left(\left(1 + r_{fu}\right) \gamma_\lambda \right)}{\bar{c}_{pr} / \left(1 + r_{fu}\right) + \bar{c}_{fu}} \tag{57}$$

where $\bar{c}_{pr}$ is the local mean concentration of reaction products. Equation 57 implies that X can be unity if the reaction products are assumed to be kept within the fine structures until a concentration is reached.

Finally, if equations 56 and 57 are combined, then the reaction rate of combustion between fuel and oxygen becomes:

$$R_{fu} = \dot{m} \,.\frac{X}{1 - \gamma^* \,.X} \,.\bar{c}_{min} \tag{58}$$

Moreover, the excess temperature of the reacting fine structures of the local mean temperature can be expressed as follows:

$$\Delta T = \frac{\Delta H_R \,.\bar{c}_{min}}{\bar{\rho} \,.C_p} \tag{59}$$

where ΔH_R is the heat of reaction and C_p is the local specific heat capacity. Finally, the temperature of the reacting fine structures T^* and the surrounding temperature T^o can be defined as below:

$$T^* = \bar{T} + \Delta T \quad and \quad T^o = \bar{T} - \Delta T \,.\, \frac{\gamma^* \,.\, X}{1 - \gamma^* \,.\, X} \tag{60}$$

where $\bar{T}$ is the local time mean temperature.

3.6. Discrete Ordinates Model (DO)

Another model is required to calculate the radiative heat transfer in the combustion chamber. Discrete Ordinates method is one of the most popular radiation calculation techniques. In this method, the heat transfer equation is solved in n directions in 4π solid angle. Moreover, the integrals are replaced by numerical quadrature. Then, the heat transfer equation becomes [27]:

$$\hat{s}_i \nabla I(r, \hat{s}_i) = \kappa(r) I_b(r) - \beta(r) I(r, \hat{s}_i) + \frac{\sigma_s(r)}{4\pi} \sum_{j=1}^{n} w_j I(r, \hat{s}_j) \varphi(r, \hat{s}_j, \hat{s}_i) \tag{61}$$

$$i = 1,2, \dots, n$$

and the boundary conditions are:

$$I(r_w, \hat{s}_i) = \in (r_w) I_b(r_w) + \frac{\rho(r_w)}{\pi} \sum_{\hat{n}.\hat{s}_i < 0} w_j \, I(r_w, \hat{s}_j) \left| \hat{n} \,.\, \hat{s}_j \right|, \quad \hat{n}.\hat{s}_i > 0 \tag{62}$$

where $\hat{s}_i$ is the unit vector in direction i, I is the intensity of radiation, r is the radial coordinate, κ is the absorption coefficient, I_b is the Blackbody intensity, β is the extinction coefficient, σ_s is the scattering coefficient, w_j is quadrature weights, φ is scattering phase function r_w is the point of the wall where the boundary condition is applied, $\in$ is the emissivity, ρ is the reflectivity and $\hat{n}$ is the unit surface normal.

Equation 61 and 62 produce a set of n first-order linear partial differential equations for the solution of intensity in given position vector and direction $(I(r, \hat{s}_i))$. This set of partial differential equations can be solved numerically.

When the intensities are determined, the radiative heat flux q in the medium can be found from equation 63:

$$q(r) = \int_{4\pi} I(r, \hat{s})\, \hat{s} d\Omega \cong \sum_{i=1}^{n} w_i I_i(r) \hat{s}_i \tag{63}$$

where Ω is the solid angle.

In the same way, the incident radiation G is calculated from equation 64:

$$G(r) = \int_{4\pi} I(r, \hat{s})\, \hat{s} d\Omega \cong \sum_{i=1}^{n} w_i I_i(r) \tag{64}$$

Heat flux at a surface may be determined from a surface energy balance:

$$q \,.\, \hat{n}(r_w) = \in (r_w)[\pi I_b(r_w) - H(r_w)] \cong \in (r_w) \left(\pi I_b(r_w) - \sum_{\hat{n}.\hat{s}_i<0} w_i\, I_i(r_w) |\hat{n}\, .\, \hat{s}_i| \right) \tag{65}$$

where H is the irradiation onto a surface.

3.6.1. Weighted Sum of Grey Gases Model

The weighted sum of grey gases model takes into account particular absorption bands and simplifies the calculation of emissivity and absorption coefficient [28]. The total emissivity over the distance s can be calculated as shown in equation 66:

$$\in = \sum_{i=0}^{I} a_{\in,i}(T)(1 - e^{-\kappa_i p s}) \tag{66}$$

where $a_{\in,i}$ is the emissivity weighting factor for the ith fictitious grey gas, T is temperature κ_i is the absorption coefficient of the i the grey gas, p is the sum of partial pressures of all absorbing gases and s is the path length.

The most common approximation for temperature dependence of $a_{\in,i}$ is:

$$a_{\epsilon,i} = \sum_{j=1}^{J} b_{\epsilon,i,j} T^{j-1} \tag{67}$$

where $b_{\epsilon,i,j}$ are the emissivity gas temperature polynomial coefficients. If the medium is not optically thin and the wall temperature is not very different from the gas temperature, it can be assumed that the emissivity is equal to the absorptivity α.

$$\epsilon = \alpha \tag{68}$$

$b_{\epsilon,i,j}$ and κ_i does not depend strongly on ps and T. Therefore, they can be assumed constant for a wide range of ps and T values. Moreover, if the total gas pressure is assumed to be 1 and if $\kappa_i ps \ll 1$, total emissivity equation becomes simplified:

$$\epsilon = \sum_{i=0}^{I} a_{\epsilon,i} \kappa_i \, ps \tag{69}$$

In the end, the grey gas model with absorption coefficient can be expressed as follows:

$$\alpha = \sum_{i=0}^{I} a_{\epsilon,i} \kappa_i \, ps \tag{70}$$

where α in general cases can be defined as:

$$\alpha = -\frac{\ln(1-\epsilon)}{s} \tag{71}$$

However, the values for κ_i have to be rescaled if the total pressure of the gases is less than 0.9 or greater than 1.1. In that case, the calculation of κ_i is as follows:

$$\kappa_i = \kappa_i P_{tot}^{m} \tag{72}$$

where m is a non-dimensional value and depends on the partial pressures and temperature of the absorbing gases and total pressure.

3.7. NO Models

The mechanisms of formation of NO can be categorized into five groups namely thermal NO route, prompt NO route, fuel nitrogen route, NO_2 route and N_2O route [29]. In this study, fuel nitrogen route is not considered because the fuel is nitrogen-free. In the simulation software, thermal NO, prompt NO and N_2O path NO mechanisms are considered to predict NO emissions.

3.7.1. Thermal NO Mechanism

Thermal NO path plays a significant role in NO_x formation if the fuel is nitrogen-free such as methane. It becomes an important mechanism in high temperature fields. Thermal NO mechanism is known by Zel'dovich mechanism. The mechanism consists of three reactions illustrated below [27]:

$$O + N_2 \underbrace{\overset{k_{1f}}{\rightleftharpoons}}_{k_{1b}} NO + N$$

$$k_{1f} = 1.8 * 10^{11} \exp\left(-\frac{38370}{T}\right) \quad \frac{m^3}{kmol.s} \tag{73}$$

$$k_{1b} = 3.8 * 10^{10} \exp\left(-\frac{425}{T}\right) \quad \frac{m^3}{kmol.s} \tag{74}$$

$$N + O_2 \underbrace{\overset{k_{2f}}{\rightleftharpoons}}_{k_{2b}} NO + O$$

$$k_{2f} = 1.8 * 10^{10} \exp\left(-\frac{4680}{R_u T}\right) \quad \frac{m^3}{kmol.s} \tag{75}$$

$$k_{2b} = 3.8 * 10^{9} \exp\left(-\frac{20820}{T}\right) \quad \frac{m^3}{kmol.s} \tag{76}$$

$$N + OH \underbrace{\overset{k_{3f}}{\rightleftharpoons}}_{k_{3b}} NO + H$$

$$k_{3f} = 7.1 * 10^{10} \exp\left(-\frac{450}{T}\right) \quad \frac{m^3}{kmol.s} \tag{77}$$

$$k_{3b} = 1.7 * 10^{11} \exp\left(-\frac{24560}{T}\right) \quad \frac{m^3}{kmol.s} \tag{78}$$

3.7.2. Prompt NO Mechanism

Rapid formation of NO by prompt NO mechanism is formed due to the reactions of hydrocarbon radicals with molecular nitrogen causing the production of amines or HCN which are subsequently converted to NO. It can be an important mechanism especially in fuel-rich conditions [27]. The principal reactions of prompt NO mechanism are shown below:

$$CH + N_2 \Leftrightarrow HCN + N$$

$$CH_2 + N_2 \Leftrightarrow HCN + NH$$

$$CH_2 + N_2 \Leftrightarrow H_2CN + N$$

$$C + N_2 \Leftrightarrow CN + N$$

where the first reaction is the rate-limiting step. The fast formation of NO started by first reaction follows a reaction sequence when equivalence ratio ϕ is around 1.2:

$$HCN + O \Leftrightarrow NCO + H$$

$$NCO + H \Leftrightarrow NH + CO$$

$$NH + H \Leftrightarrow N + H_2$$

$$N + OH \Leftrightarrow NO + H$$

3.7.3. N_2O Path NO Mechanism

In lean combustion conditions, N_2O intermediate is produced then it leads to the production of NO by reacting further with the radicals. In flameless combustion this mechanism may be the most contributing mechanism depending on the temperature field inside the combustion chamber and the inlet temperature of the oxidizer. The intermediate N_2O formation occurs by the following reactions [27]:

$$NH + NO \Leftrightarrow N_2O + H$$

$$NCO + NO \Leftrightarrow N_2O + CO$$

Afterwards, the intermediate N_2O reacts further with H atoms and forms N_2:

$$N_2O + H \Leftrightarrow N_2 + OH$$

The O atom reacts with the N_2 produced and lead to the reaction below in the presence of a third body M:

$$N_2 + O + M \rightarrow N_2O + M$$

Finally, the formation of NO takes place when N_2O reacts with O atoms:

$$N_2O + O \rightarrow NO + NO$$

3.8. Computational Details

The computational mesh represents 1/16 (22.5°) of the laboratory scale mild combustor. The specified ratio 1/16 is selected because the combustor has 16 fuel nozzles around the air nozzle. The dimensions of the chamber are given in Figure 11 [5].

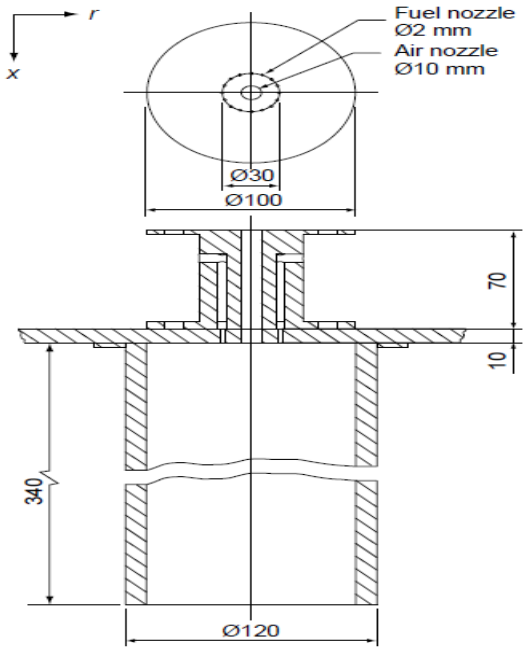

Figure 11. The schematic of the laboratory scale mild combustor

Gambit was used for the meshing and Ansys Fluent was used for the numerical simulations. The grid structure of the mesh is shown in Figure 12.

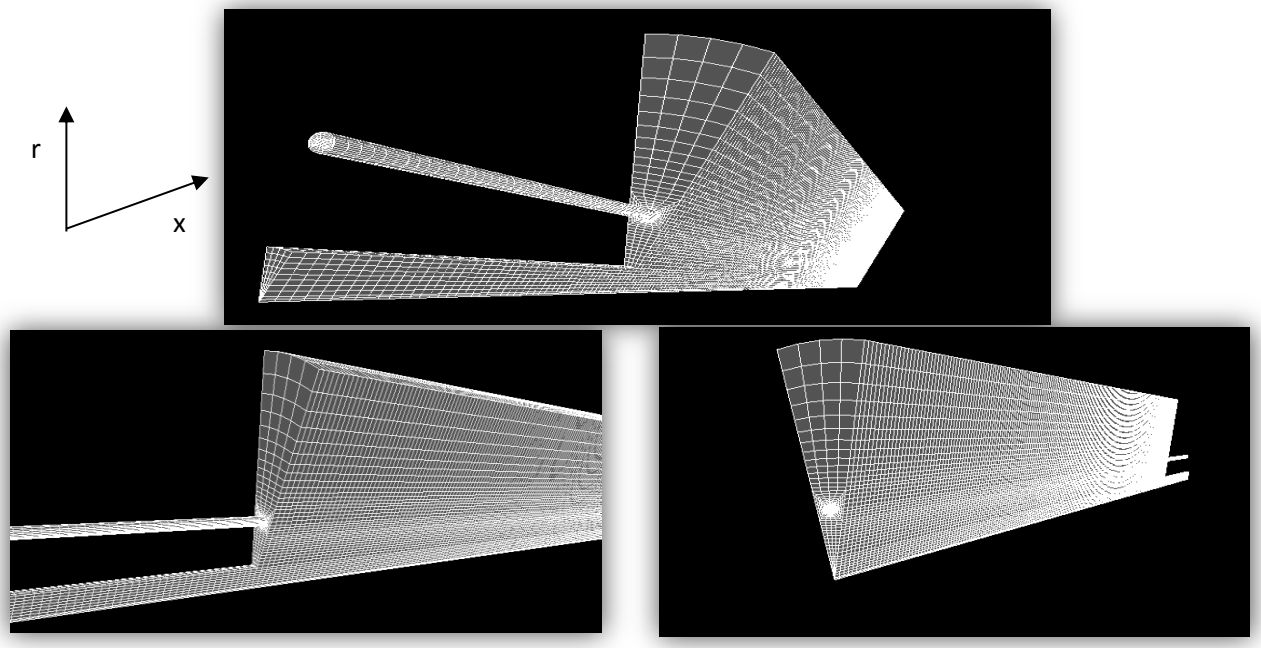

Figure 12. The coarser computational mesh

For all of the meshes, hexahedral cells were used. The size of the elements was increased in the vicinity of the cylinder wall. Especially the number of elements in the expected reaction zone was increased. Non-uniform computational domain includes around 100,000 elements for the coarser and around 400,000 elements for the finer meshes. The mesh in Figure 12 corresponds to the coarser mesh.

DRM-19 CHEMKIN mechanism was selected as the reaction mechanism for methane combustion. It includes 21 species and 84 reactions. Standard wall functions were used for near-wall treatment. The wall temperature was set to 1200 °K based on the experimental data and the operating pressure was set to atmospheric pressure for all cases. SIMPLEC algorithm was used in the simulations and all spatial discretizations of the species were solved using second order upwind scheme. Under-relaxation factors (URF) were kept as default except for one case where the turbulence was very high. For smaller air nozzle case, energy and turbulent viscosity values were decreased to 0.9 from 1.

The convergence criterion requires that the sum of the residuals decreases below a tolerance set to 10^{-3} for all of the equations except for the energy equation which was selected as 10^{-6}. The convergence criterion for Discrete Ordinates was 10^{-6} as default. The computational cost to reach that criterion value was high and the results did not vary significantly between the values of 10^{-3} and 10^{-6}. Therefore, it was set as 10^{-3}.

4. RESULTS AND DISCUSSION

4.1. Introduction

In this chapter, the results obtained from ANSYS Fluent are presented in six different sections. First of all, the influence of grid size is investigated. Then, mean temperatures and OH contours of the cases are shown and discussed. Afterwards, the effect of excess air ratio, air inlet temperature, and air nozzle size are studied and compared with the experimental data. Finally, the contributions of different NO mechanisms and the influence of the settings in NO models are discussed.

One case is selected as reference case in which the excess air ratio (λ) is 1.3, air inlet temperature is 400 °C and air nozzle diameter 10 mm. Table 2 gives brief information about the operating conditions and physical constraints:

Table 2. Operating conditions of the cases

Case	$D_{air\ nozzle}$ (mm)	λ	$T_{air\ inlet}$ (°C)	P_{fuel} (kW)	V_{fuel} (m/s)	V_{air} (m/s)
1 (Reference)	10	1.3	400	10	6.1	109.1
2	10	1.7	400	10	6.1	142.5
3	10	1.3	700	10	6.1	157.5
4	7	1.3	400	10	6.1	223.6

For all of the cases, firstly, the temperature profiles are presented both axially and radially. Then, species molar percentages namely CO_2, O_2, CO and NO are shown along the combustor.

4.2. Influence of Grid Size

In this section, the effect of grid size is investigated by comparing 100000 and 400000 elements meshes. First of all, axial and radial profiles of temperature are compared. Then, the differences between axial and radial profiles of species CO_2, O_2, CO and NO are shown. Case 1 (λ=1.3 400 °C) is taken for the grid size comparison because it is selected as reference case.

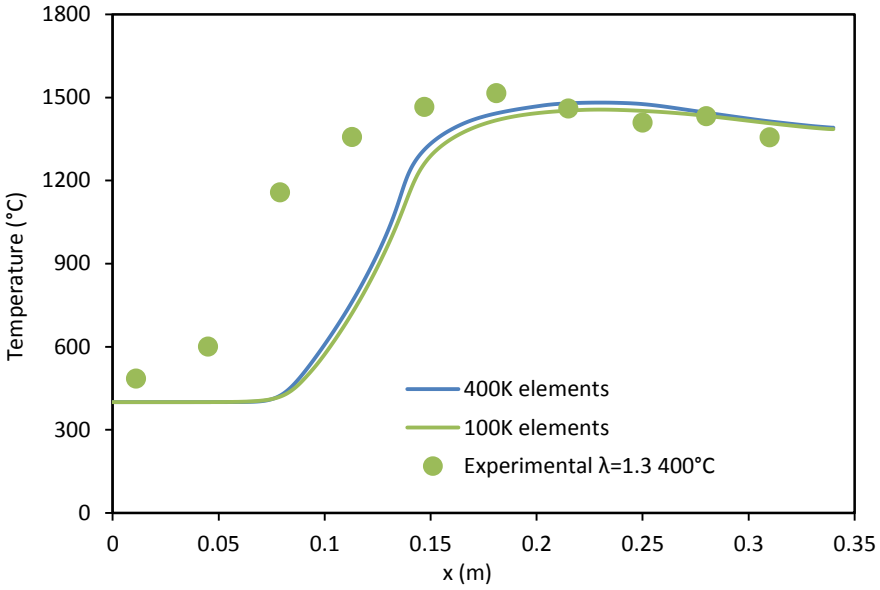

Figure 13. Axial profiles of temperature of Case 1 for different grid sizes

Figure 13 shows that the predictions of temperature for the coarser and the finer mesh are very similar. Although there are approximately four times more elements in the finer mesh, the axial temperature profiles are rather similar. Especially at the inlet and the outlet, the estimations are coincident. There is a slight difference of estimations between x=0.1 m and x=0.25 m where the finer mesh gives little higher values. Figure 14 illustrates the radial profiles for both meshes.

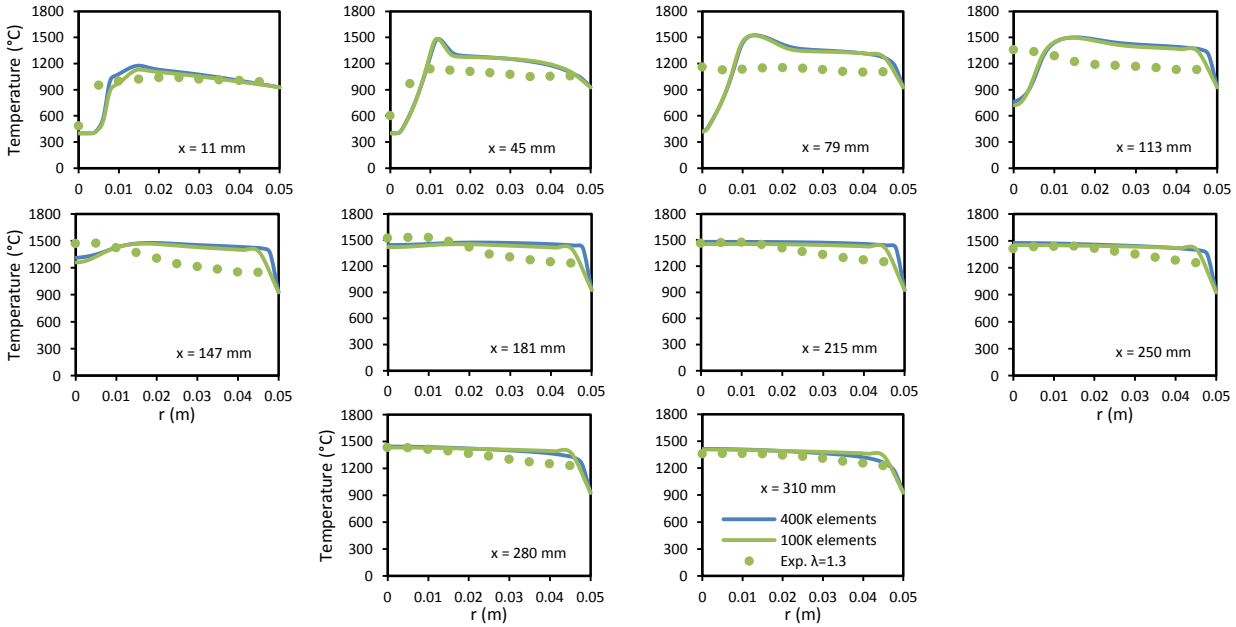

Figure 14. Radial profiles of temperature of Case 1 for different grid sizes

The radial profiles are taken at 10 different axial positions because of the available measured data. The radial profiles show that the estimations for both meshes are almost matching with each other in all of the axial points. At r=0.04 m, where it is close to the combustor wall, slight discrepancies are observed. Moreover, at x=11 mm, finer mesh gives slightly higher temperatures, whereas x=310 mm, it gives a better approximation of temperature field.

The same axial and radial profile presentation schemes are followed for species CO_2, O_2, CO and NO (see Fig. 15 and 16). The profiles are shown in molar percentages for CO_2, O_2 and CO whereas; ppm values are used for NO. However, due to space limitations, only seven radial profiles are represented instead of 10.

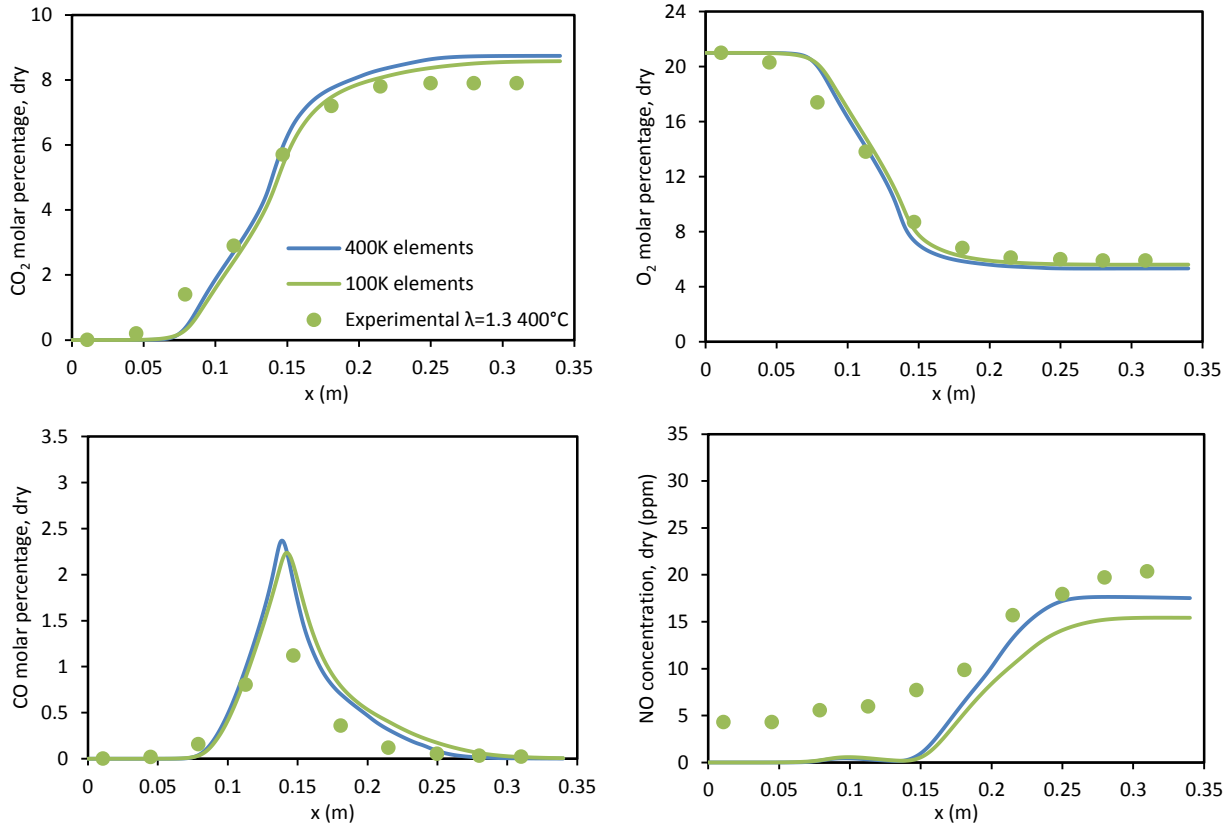

Figure 15. Axial profiles of species CO_2, O_2, CO and NO of Case 1 for different grid sizes

CO_2 and O_2 concentrations vary similarly with both finer and coarser mesh. In case of CO, finer mesh gives marginally higher peak value than coarser mesh. On the other hand, NO estimations are different. Finer mesh ends up with a better approximation of NO concentration which is 2-3 ppm higher than coarser mesh at the outlet.

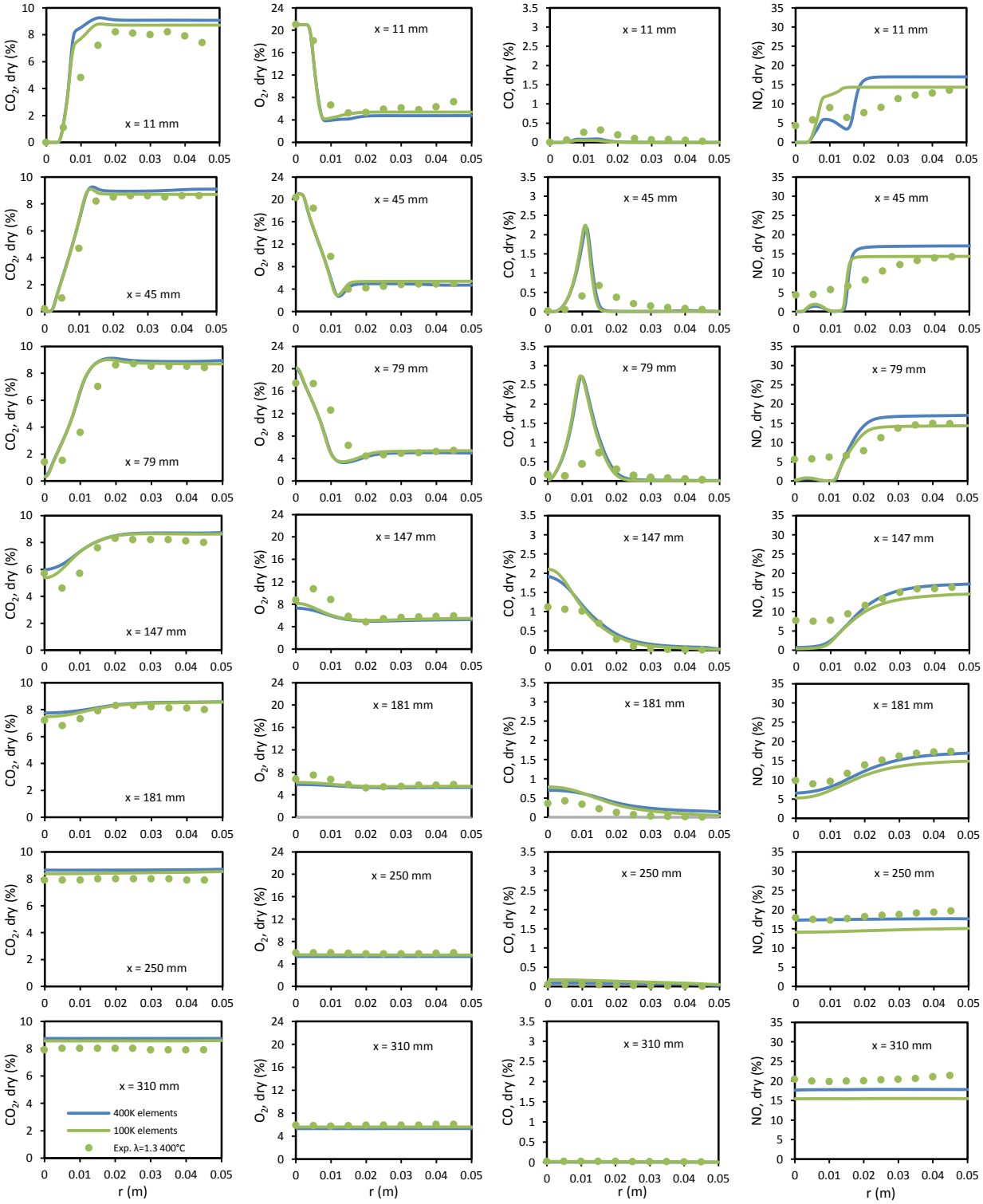

Figure 16. Radial profiles of species CO_2, O_2, CO and NO of Case 1 for different grid sizes

The radial profiles of CO_2, O_2, and CO show that the change in grid size did not affect the species molar fractions. In almost all of the radial profiles, both meshes give similar estimations. However, NO estimations are very different at x=11 mm. After that point, they give similar results. At x=310 mm, which is the closest point to the outlet, finer mesh gives 2-3 ppm better approximations due to higher oxygen radial concentration. The slight differences in molar fractions of the species might also be caused by different concentrations of hexahedral elements in the meshes. Sometimes, it may lead to worse estimations if the mesh is not generated uniformly. The comparison of grid size shows that the difference of estimations in temperature and the species is insignificant. Therefore, the rest of the comparisons are done based on the coarser mesh.

4.3. Mean Temperatures and OH Contours

Experimental mean temperatures of each cases were calculated based on averaging 50 measurements taken along the combustor. On the other hand, predicted mean temperatures were calculated using volume integral of static temperaure in the simulation software. Table 2 shows the predicted and experimental data along with the relative error.

Table 3. Predicted and experimental mean temperature values

Case	Predicted mean temp. (°C)	Experimental mean temp. (°C)	Relative Error (%)
1 (Reference)	1333	1240	7.5
2	1239	1218	1.7
3	1405	1357	3.54
4	1278	1233	3.65

The highest deviation is observed in the reference case with 7.5 relative error, while the least deviation is seen in Case 2. It is also shown that the lowest predicted and experimental mean temperature values are observed in Case 2. Moreover, the increase of air inlet temperaure leads to approximately 70 °C increase in predicted mean temperature compared to the reference case. However, the decrease in air nozzle diameter causes the predicted mean temperature to decrease 55 °C.

Predictions of the molar OH fractions are investigated to identify the reaction zones based on OH intensities. The contours showing the molar fractions are represented in Figure 17.

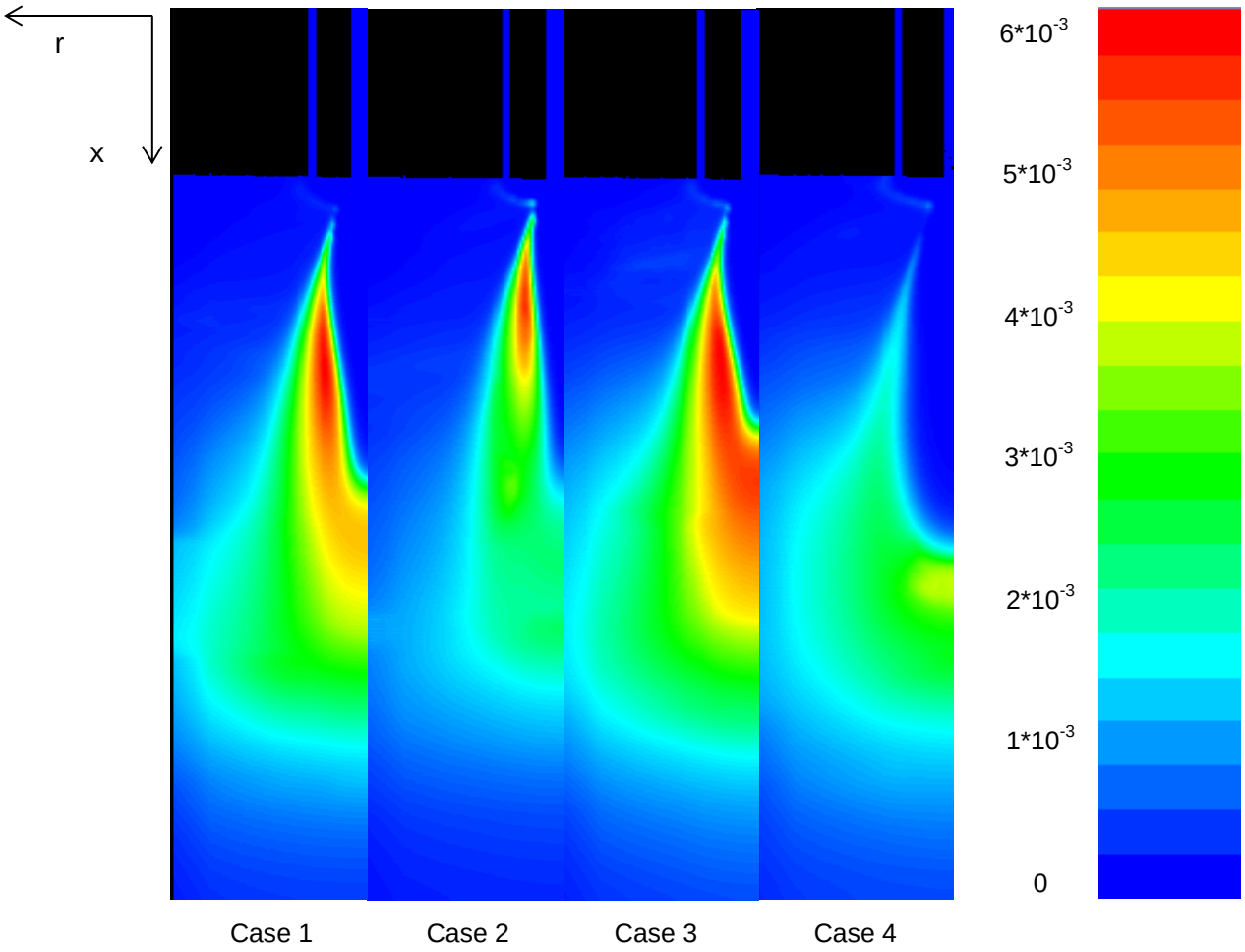

Figure 17. Contours of the OH mole fractions of the cases

The contours of Case 2 show that the increase in excess air ratio leads to a smaller reaction zone, which is shifted towards the burner compared to Case 1 where OH intensity is also lower. Air inlet temperature increase in Case 3 causes higher OH intensity in a certain area. Moreover, the reaction zone in Case 3 is observed as the largest. In Case 4, the size of the reaction zone is smaller than Case 1. In addition to that, OH intensity in Case 4 is the lowest of all cases.

4.4. Influence of Excess Air

The effects of operating conditions are shown by comparing the reference case with the relevant cases including the experimental data. Concerning excess air ratio, the value is increased from 1.3 to 1.7 while the other parameters are kept constant. Namely, Case 1 and Case 2 are compared. The axial profiles of temperature are shown in Figure 18.

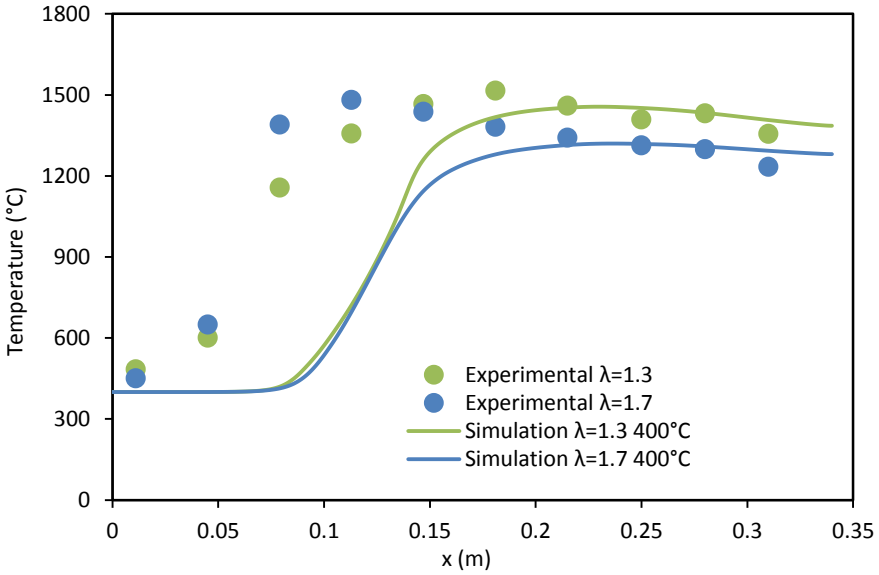

Figure 18. Axial profiles of temperature of Case 1 and Case 2

Both cases have a similar trend of temperature profile for simulations, where they dramatically increase after 0.1 m of the combustor. However, they are not coincident with the experimental data until the middle of the chamber. Moreover, it can be seen that with the lower excess air ratio, higher temperature field is observed. The peak temperature difference in simulations is around 200 °C. Radial temperature profiles of predicted and measured data are illustrated in Figure 19.

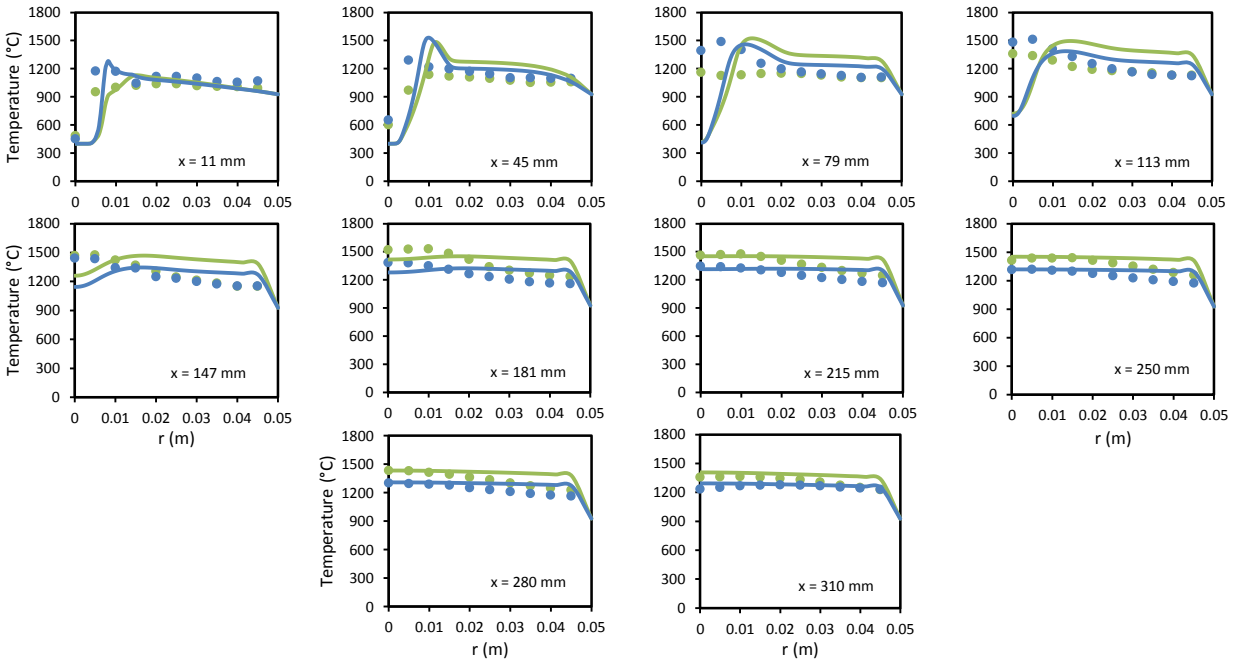

Figure 19. Radial profiles of temperature of Case 1 and Case 2

It is seen from Figure 19 that simulation of Case 1 gives around 100 °C higher values of estimations than Case 2 throughout the combustor except in the vicinity of the burner. Moreover, the estimations around the burner zone are not very accurate. For instance, the predictions at x=79 mm and x=113 mm are not very good until 0.01 m of radial distance. Outlet temperatures are predicted well enough especially for the case with higher excess air ratio.

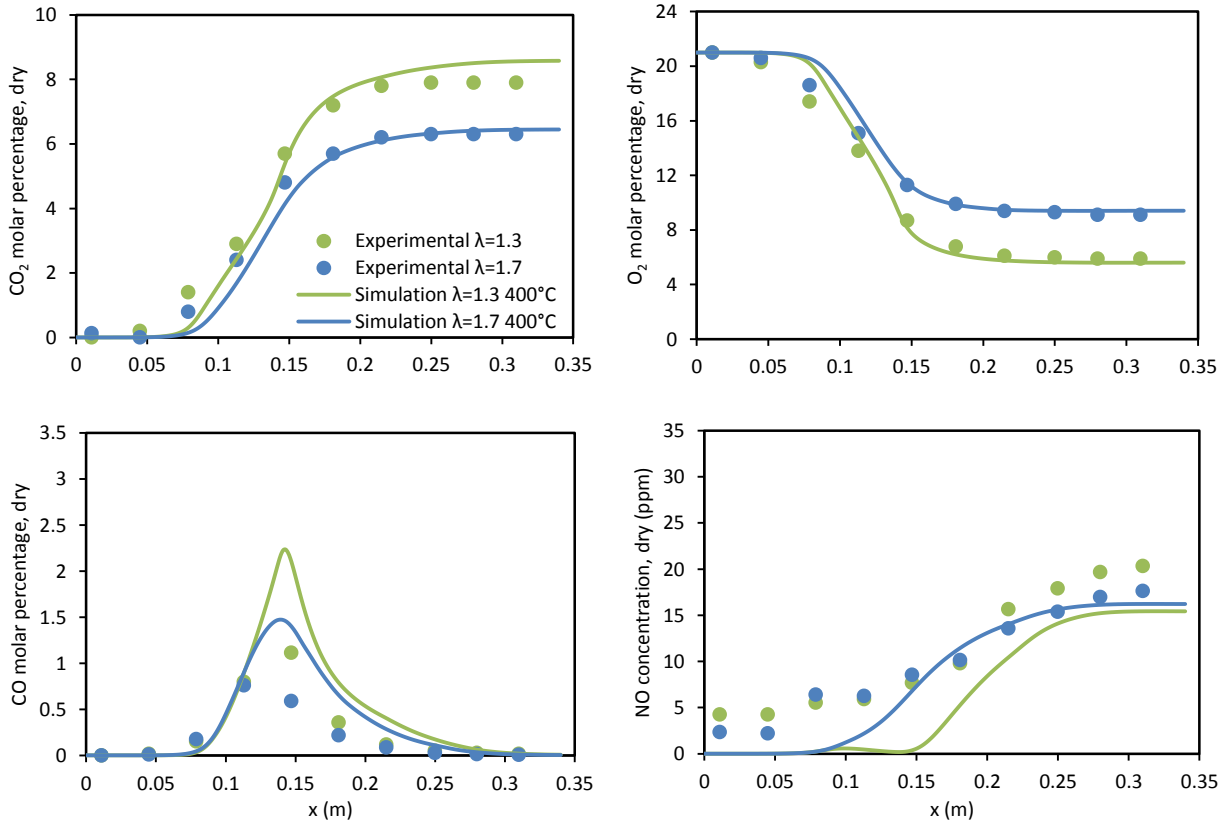

Figure 20. Axial profiles of species CO_2, O_2, CO and NO of Case 1 and Case 2

The predictions of molar percentages of CO_2 and O_2 displayed in Figure 20, are in a good agreement with the experimental data for both cases. For lower λ, higher CO_2 concentrations are predicted compared to higher λ, due to the dilution of the flue gases by higher amount of inlet air in the latter case. On the contrary, lower O_2 concentrations are observed for lower λ. In case of CO, generation of CO occurs close to the middle of the combustion chamber and it decreases when λ increases. NO concentrations increase towards the exit. Experimental data shows that the emission of NO becomes lower if λ increases. This behaviour is not well estimated in the simulations. However, experimental differences are very small and the accuracy of the model is limited.

Figure 21 shows the profiles of the species radially in seven different axial points.

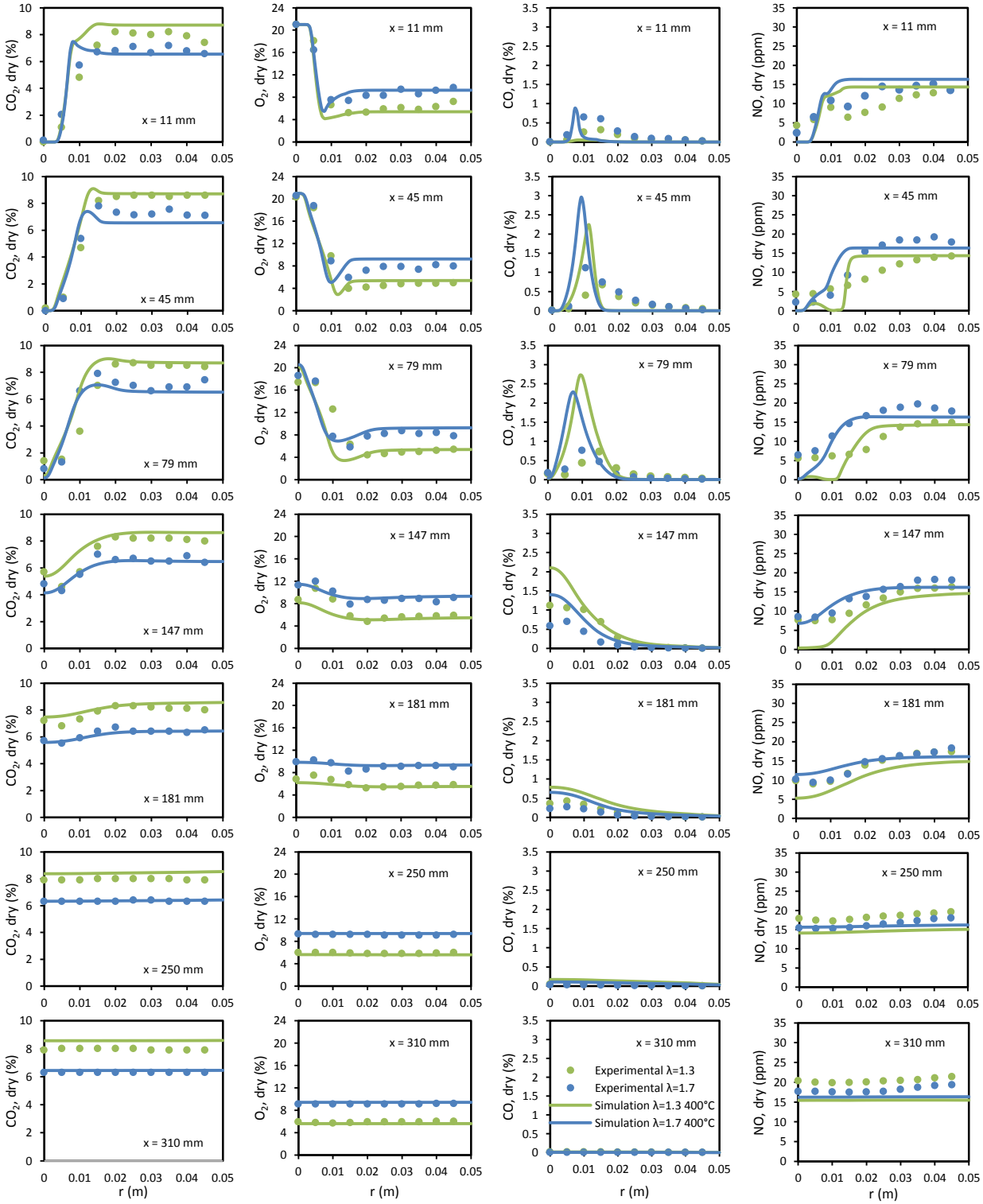

Figure 21. Radial profiles of species CO_2, O_2, CO and NO of Case 1 and Case 2

It is seen that CO_2 and O_2 molar percentages in dry basis are in good conformity with the experimental data. Despite this, CO concentration is higher at x=11 mm and x =45 mm and it gradually decreases in the vicinity of the exit. NO predictions are good especially for the case with higher λ. Overall, for all species, the predictions of the radial profiles become more accurate results as the outlet of the combustor is approached.

4.5. Influence of Air Inlet Temperature

Air inlet temperature may have a significant effect on the flameless combustion. It has an effect on the temperature distribution thus, pollutant formation. In this section, Case 1 (λ =1.3 and T_{air}=400°C) and Case 3 (λ =1.3 and T_{air}=700°C) are compared in Figure 22 and 23, which show axial and radial profiles, respectively.

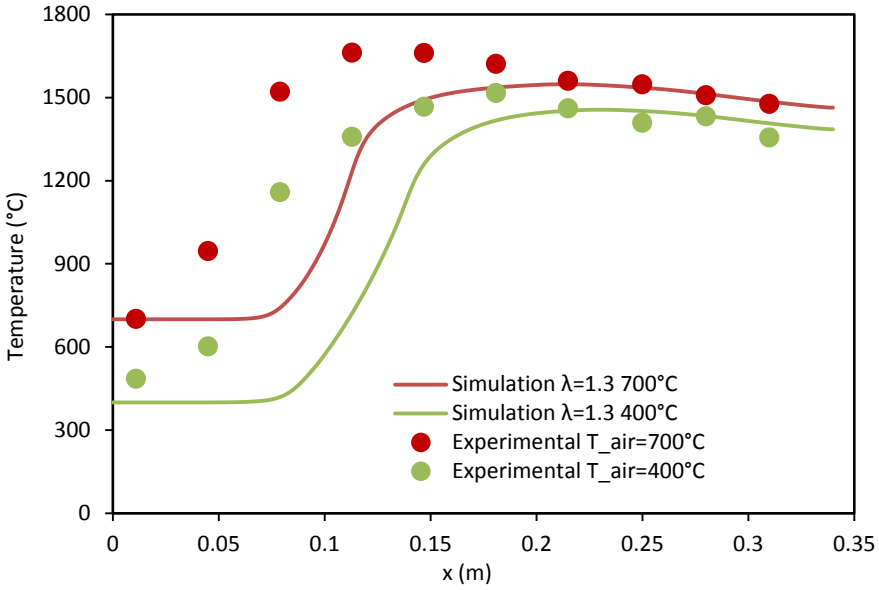

Figure 22. Axial profiles of temperature of Case 1 and Case 3

The increase of air inlet temperature leads to high temperatures around 1600 °C inside the combustor. In the outlet around 100 °C difference is observed. The predictions are not very accurate close to the burner zone. The deviations of both simulations from the experimental data are similar. Radial profiles are shown in Figure 23.

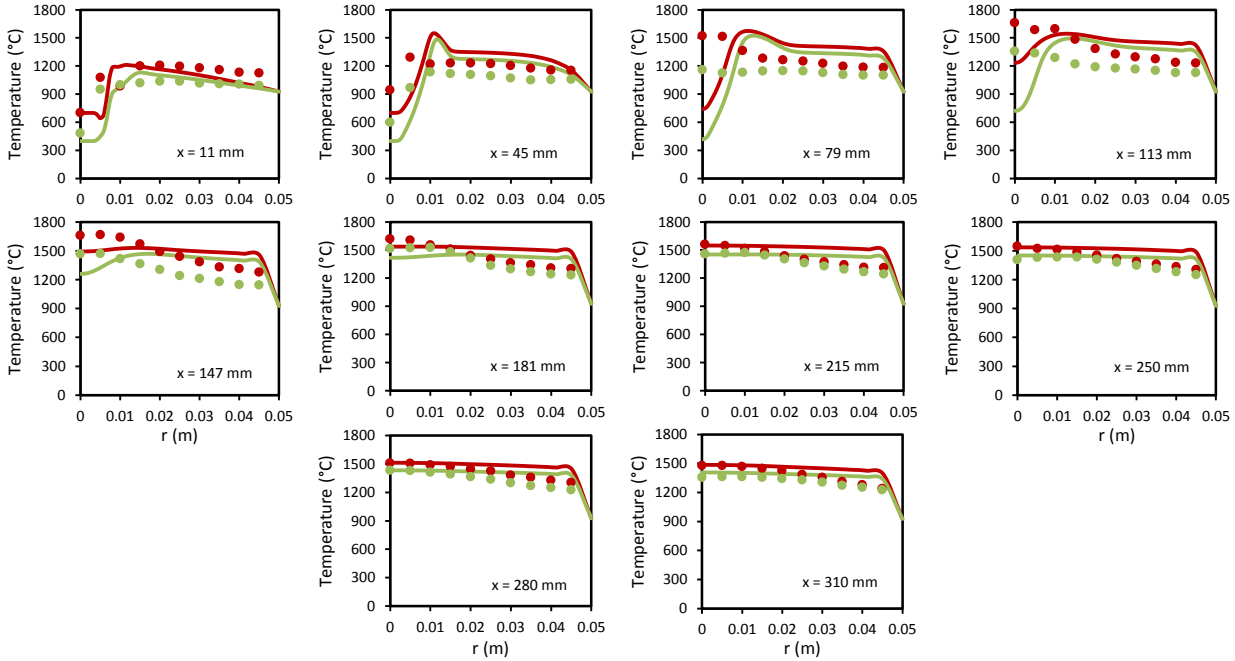

Figure 23. Radial profiles of temperature of Case 1 and Case 3

The radial profiles show that the increase from 400 °C to 700 °C of the air inlet temperature caused a rise of the temperature field by approximately 100 °C throughout the combustor. It can be observed that in both cases, the accuracy of the predictions is not good particularly at x=79 mm and x=113 mm. Furthermore, especially where x=280 mm and x=310 mm, the predictions of both cases gets worse as the radial distance increases. However, this deviation is not significant.

Figure 24 displays the axial profiles of species molar fractions. It is seen that the predicted outlet CO_2 and O_2 molar percentages are in good agreement due to the accurate estimation of the stoichiometry. The maximum predicted CO concentration is slightly higher in Case 3. For CO_2, O_2, and CO the predictions are not coincident except in the vicinity of the inlet and the outlet. The reason might be the difference of the air inlet temperatures to the combustor. In case of NO, there is an observable increase in the concentration of NO particularly closer to the outlet. It appears that the contribution of thermal mechanism in Case 3 is greater than in Case 1. In addition, NO concentration is estimated more accurately in Case 3 than Case 1.

Radial profiles of species CO_2, O_2, CO and NO are shown in Figure 25.

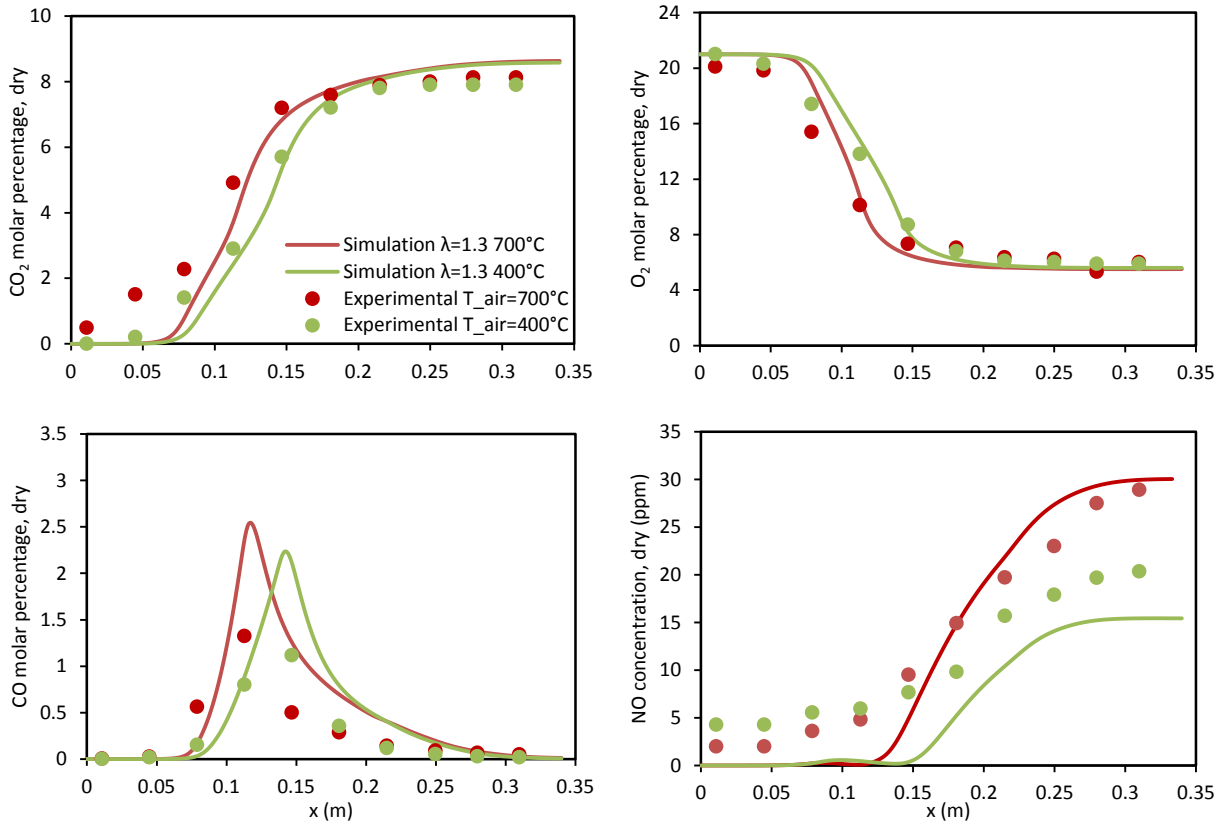

Figure 24. Axial profiles of species CO_2, O_2, CO and NO of Case 1 and Case 3

The predictions of the radial profiles of the species show that CO_2 and O_2 concentrations do not differ significantly from the experimental data. Moreover, the predictions of CO_2 and O_2 are coincident for almost all radial profiles due to correct stoichiometry calculations. CO mole fractions are decreasing and become almost zero while getting closer to the outlet. NO_x predictions for Case 3 are not well estimated in the burner zone up to x=147 mm. After the middle of the combustor, the predictions of NO become more accurate.

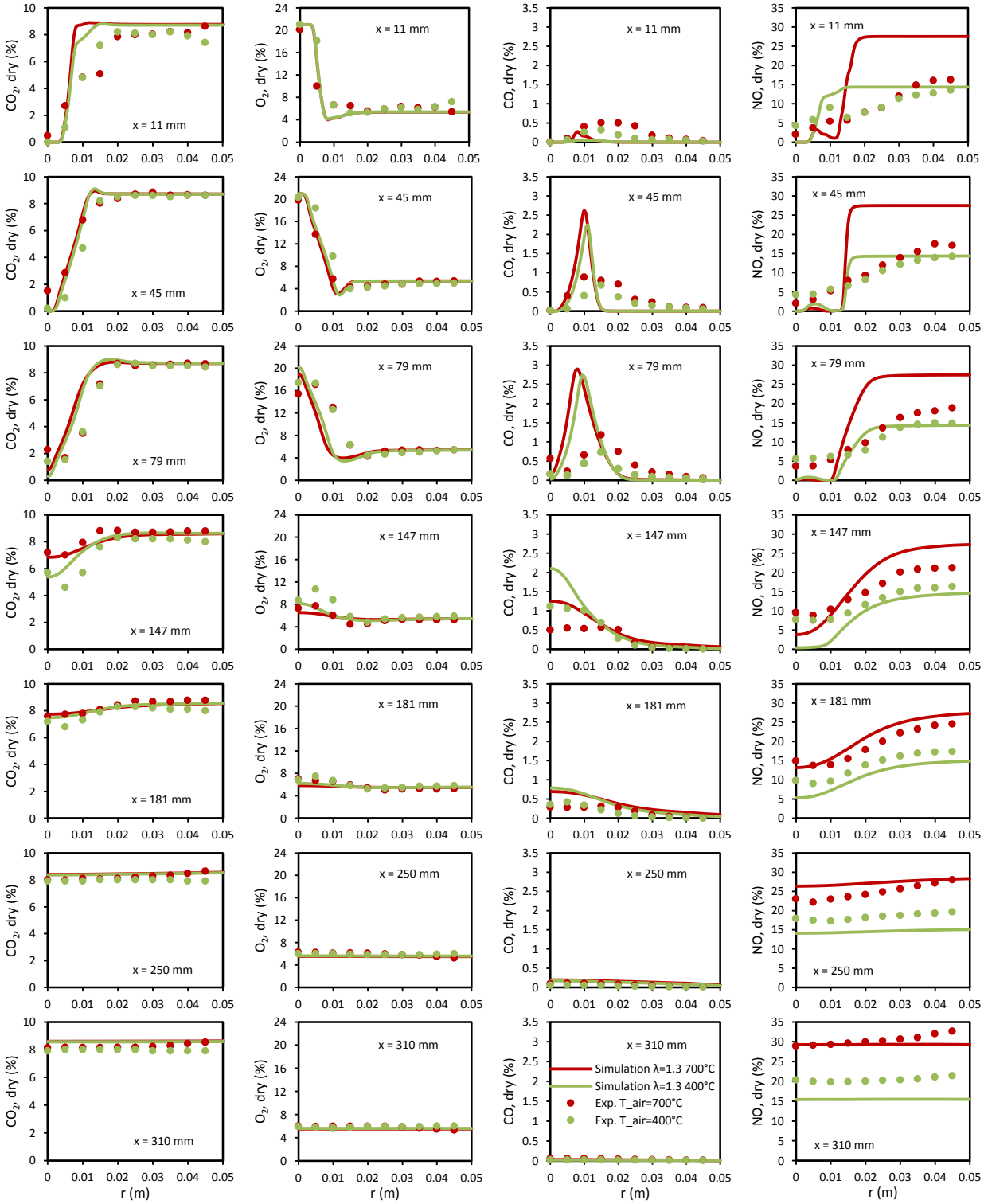

Figure 25. Radial profiles of species CO_2, O_2, CO, NO of Case 1 and Case 3

4.6. Influence of Air Nozzle Diameter

Next investigation is done by decreasing the diameter of the air nozzle from 10 mm to 7 mm and keeping the excess air ratio and air inlet temperature constant. Due to contraction, the air inlet velocity increases dramatically from 109.1 m/s to 223.6 m/s. Therefore it has a great effect on turbulence, temperature field and species concentrations. The analysis is done using the same method which includes the investigation of temperature field and the species concentrations both axially and radially. Axial profiles of temperature of Case 1 (λ = 1.3 and D_{air} = 10 mm) and Case 4 (λ = 1.3 and D_{air} = 7 mm) are illustrated in Figure 26.

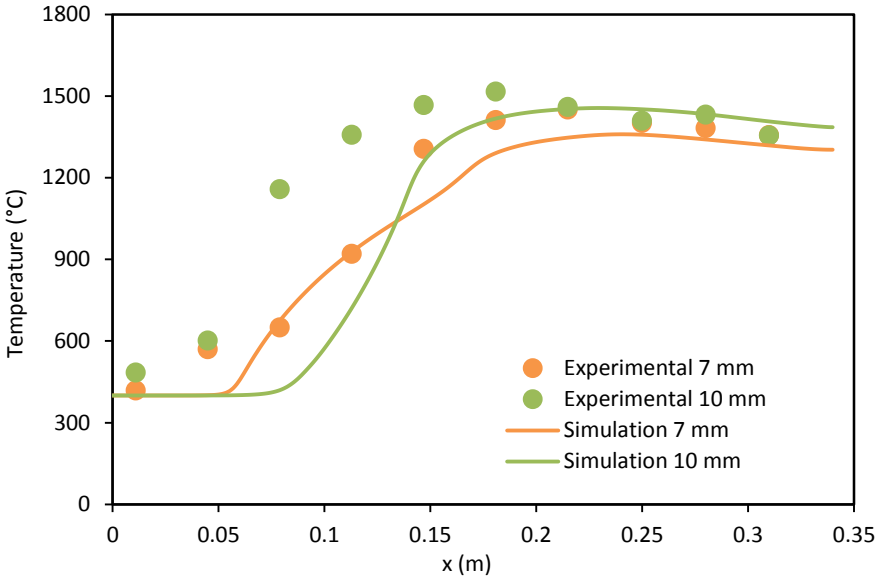

Figure 26. Axial profiles of temperature of Case 1 and Case 4

The predictions in Figure 26 show that the axial temperature field with smaller air nozzle diameter is in better agreement with the experimental data than the other case. It is seen that the big gap of Case 1 simulation and experimental data around the burner zone almost disappears in Case 4. Furthermore, more than 100 °C decrease at the outlet of the combustor is observed. The radial temperature profiles are presented in Figure 27.

The radial profiles show that the increase of the air inlet velocity decreases small peaks of temperature occurring in the combustor. The main cause of this occurrence might be better mixing and more efficient combustion in the system. Closer to the outlet where x = 250 mm and x = 310 mm, the experimental data almost coincide whereas the estimations have a slight difference around 70 °C.

Subsequently, the species concentrations are compared based on the experimental and simulation data in Figure 28.

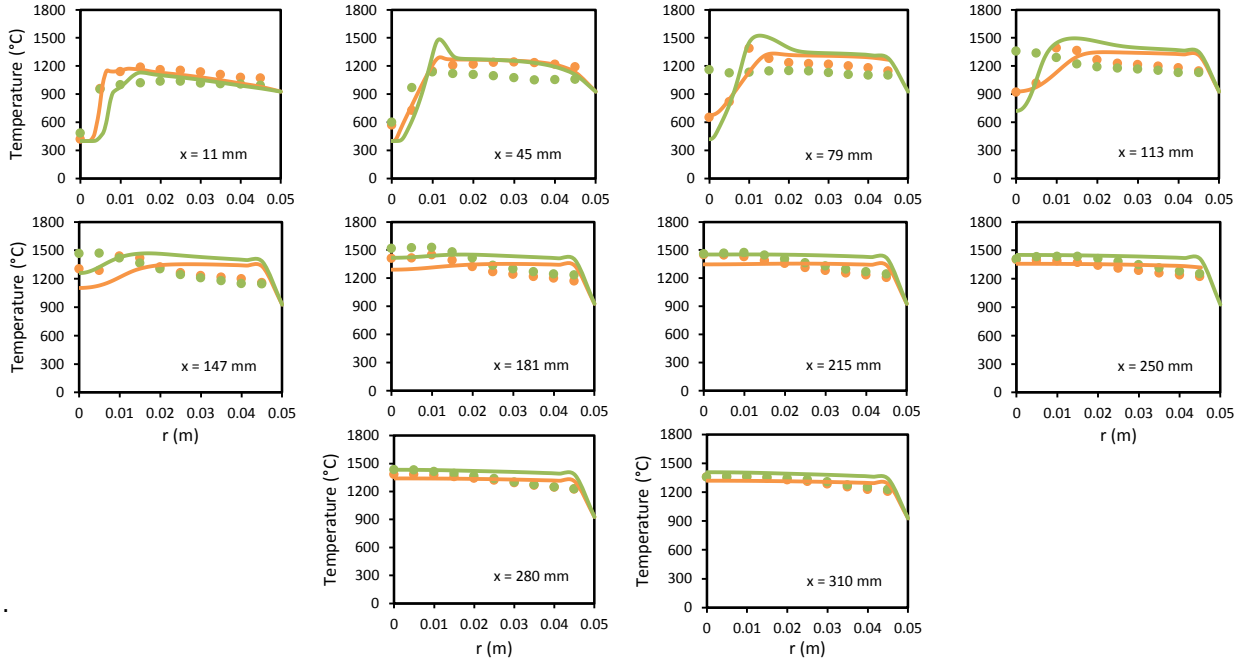

Figure 27. Radial profiles of temperature of Case 1 and Case 4

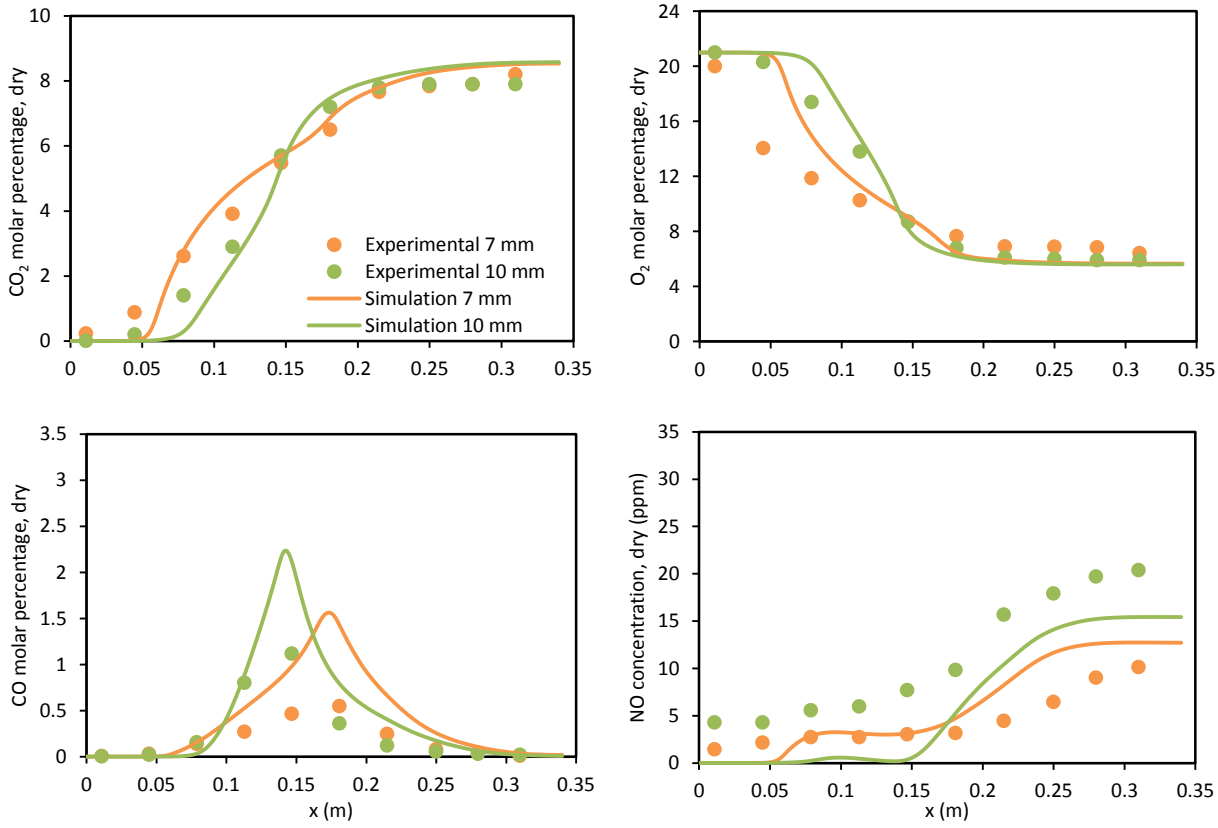

Figure 28. Axial profiles of species CO_2, O_2, CO and NO of Case 1 and Case 4

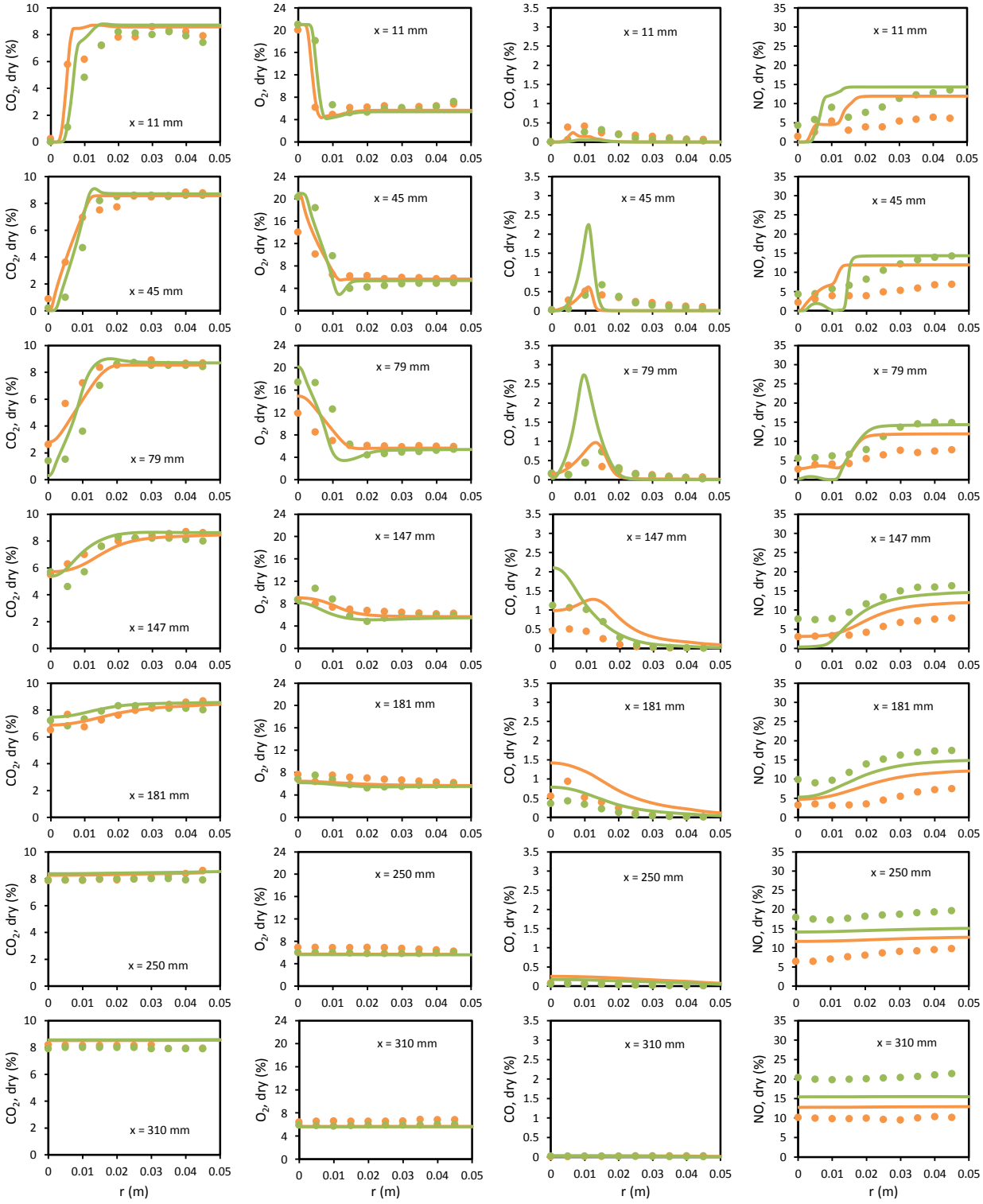

Figure 29. Radial profiles of species CO_2, O_2, CO, NO of Case 1 and Case 4

It is clear that the estimated outlet concentrations of CO_2 and O_2 are almost the same, as expected because both cases have the same λ. Moreover, the variations of the molar percentages of all the species are lesser with 7 mm air nozzle diameter. For instance, the peak CO molar percentage is around 1.5 per cent in Case 4 while it is close to 2.5 per cent in Case 1. Additionally, NO concentration reduces significantly to about 10 ppm emission.

Lastly, the radial concentrations of the species are shown in Figure 29.

CO_2 and O_2 radial profiles of Case 4 show that the concentrations of species become more uniform with the reduction of the diameter. In case of CO, similar behavior is observed in which the increase in CO concentration around the burner zone is smaller than in Case 1. NO_x estimations are not very accurate for the burner zone for both cases. On the other hand, NO_x concentration at the point closest to the outlet is predicted as 12-13 ppm whereas the experimental data is around 10 ppm.

4.7. Influence of NO Mechanisms and Parameters

In this section, the contribution of thermal, prompt and N_2O path mechanisms in all of the cases are investigated. For each case, one axial profile showing the contributions of the mechanisms is presented. Moreover, the effects of changing parameters in NO analysis are observed by including all of the mechanisms. First of all, the axial profile showing the contribution of each mechanism of the reference case (λ = 1.3 and T_{air} = 400°C) is illustrated in Figure 30.

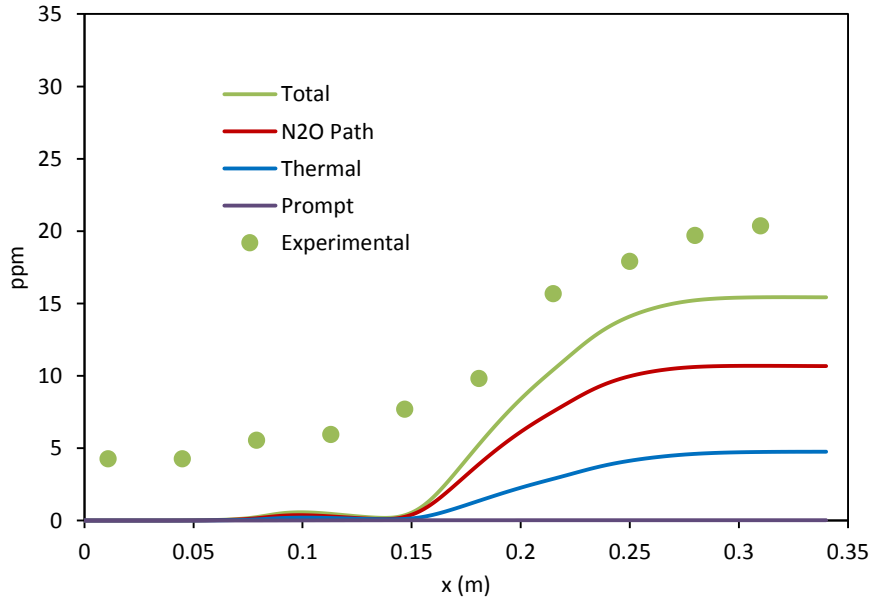

Figure 30. Axial profiles of NO concentrations of individual mechanisms for Case 1

It is seen that N_2O path has the highest contribution in this case. The share of thermal NO is around 35 % whereas the role of prompt mechanism is almost negligible. It is expected to have a higher share of N_2O path in flameless combustion because of having more uniform conditions in combustion chamber. The results are compatible with this argument.

Subsequently, the axial profiles of Case 2 are presented in Figure 31;

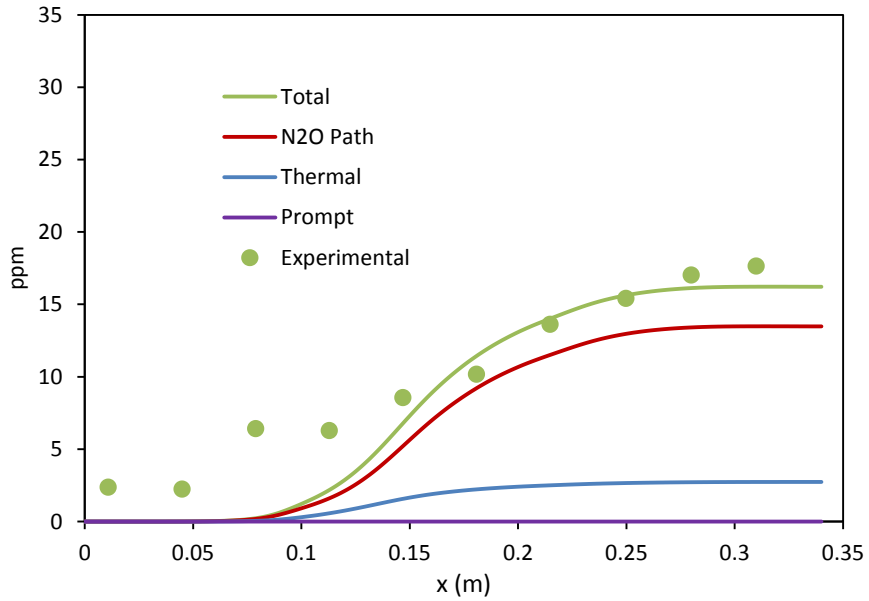

Figure 31. Axial profiles of NO concentrations of individual mechanisms for Case 2

In Case 2, the effect of excess air ratio on NO mechanisms is observed to be significantly. When it is increased from 1.3 to 1.7, N_2O Path mechanism becomes the determining mechanism of the total NO production. As in Case 1, prompt mechanism has almost no contribution to the emission. However, thermal mechanism has around 15 % contribution of total.

Figure 32 represents the influence of air inlet temperature on NO mechanisms. It is clear that the contribution of thermal mechanism becomes almost the same with N_2O path mechanism when air inlet temperature is increased from 400 °C to 700 °C. However, N_2O path is still observed as the dominating mechanism throughout the combustor.

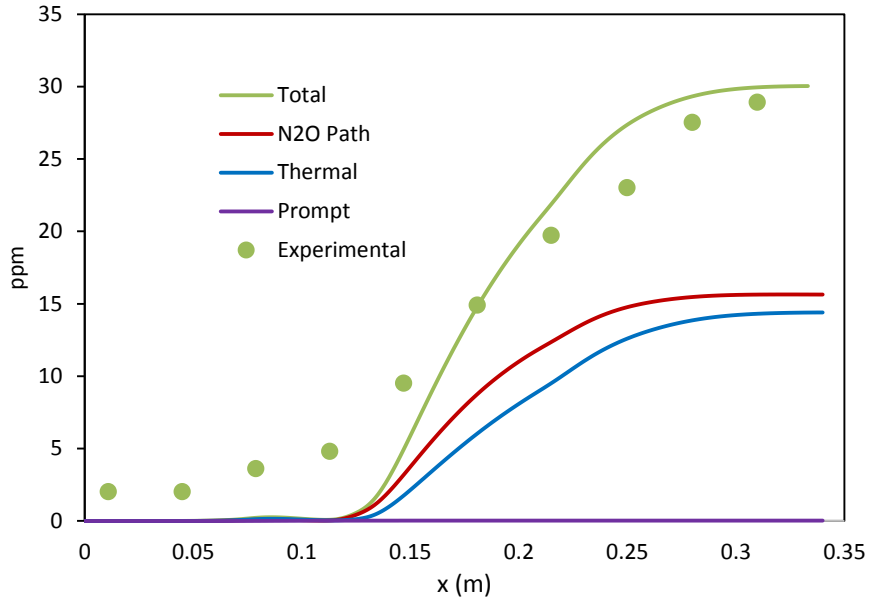

Figure 32. Axial profiles of NO concentrations of individual mechanisms for Case 3

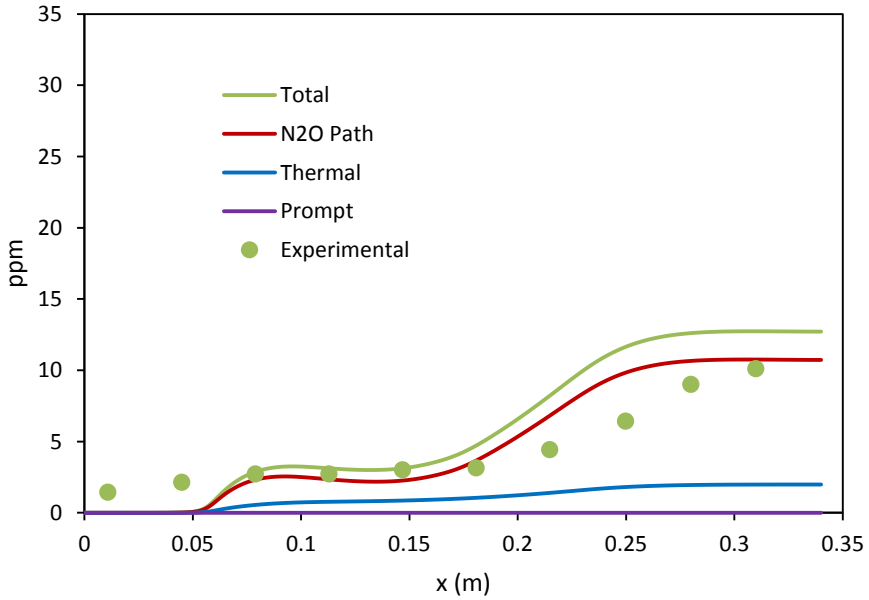

Figure 33. Axial profiles of NO concentrations of individual mechanisms for Case 4

Figure 33 demonstrates that N_2O path mechanism is dominant in case of using 7 mm air nozzle diameter. The contribution of thermal mechanism is around 10 % while the influence of prompt mechanism is almost zero. Even though Case 4 has the same excess air ratio and air inlet temperature, total NO fractions are different. Moreover, the share of each mechanism is also different. The share of N_2O path increases when air nozzle contraction is applied. Therefore, it can be said that turbulence has also a significant effect on NO_x production and mechanisms.

In all of the cases, N_2O path mechanism is observed to be the highest contributing mechanism to total NO production. The share of thermal mechanism is less than 1/3 of the total production, except for Case 3 where it is almost equal to N_2O Path mechanism. In all cases, prompt mechanism has almost no contribution to the production. This might be caused by having high enough excess air. Because prompt mechanism has higher influence in rich flames.

In thermal NO analysis, [O] and [OH] models were taken as (instantaneous option in Ansys Fluent), the concentrations calculated from the combustion model. Equilibrium and partial-equilibrium approaches for the estimations of [O] and [OH] gave much worse estimations. For instance, when equilibrium or partial-equilibrium approaches were used, the estimations decreased from 30 ppm to 5-6 ppm, which is far from the experimental values. This significant effect occurs because [O] model was also used in N_2O path model.

Since the most important mechanism was N_2O path, two approaches were used to optimize the calculation of the mechanism. In quasi-steady model, no transport equation for the species N_2O is solved whereas in transported-simple model, mass fraction of N_2O is calculated from the solution of its transport equation. After several trials with both methods, it was concluded that the quasi-steady model gave slightly better approximations without compromising the computation cost. Therefore, the quasi – steady model was used in all of the simulations to predict the N_2O path mechanism.

In NO post-processing, the turbulence interaction mode was activated both for temperature and species. The assumed shape of the PDF type was changed from ‘beta’ (default) option to ‘gaussian’ option due to worse estimations of the former in Case 3. Changing temperature variance option from ‘algebraic’ to ‘transported’ resulted a higher computation cost without getting better estimations. Moreover, a similar behavior was observed when T_{max} option was changed from ‘global’ to ‘local’.

Turbulence interaction mode for species is set as O_2 default in Ansys Fluent. The setting was changed to ‘N_2’ and ‘O’ to observe the effect. In both cases, the changes yielded an over estimation for the reference case. For instance, 15 ppm NO concentration was achieved with ‘O_2’ interaction however it increased to 35 ppm by selecting ‘N_2’ and ‘O’ interaction respectively, which is far from the experimental data.

5. CONCLUSIONS

A mild laboratory combustor was computationally simulated to examine the influence of the operating conditions. Four different cases were considered by changing three parameters namely, excess air ratio, air inlet temperature and air inlet nozzle diameter. The cases were numerically investigated and compared with the experimental data.

In terms of mathematical modeling, the realizable k- ε model was used for the turbulence closure. Eddy Dissipation Concept was used with DRM-19 skeletal mechanism for the combustion modeling. The simulations were carried using the commercial code Ansys Fluent with two different mesh sizes. The effects of the operating conditions were observed by examining the temperature fields, CO_2, O_2, CO and NO molar fractions both axially and radially. The results showing the influence of the operating conditions were represented by the coarser mesh due to insignificant effect of the grid size.

First of all, excess air ratio was increased from 1.3 to 1.7 by keeping other parameters constant. It was observed that excess air ratio increase caused a decrease of the mean temperature by about 100 °C according to the simulation results. CO_2 molar fractions decreased while O_2 molar fractions increased due to the dilution of the flue gases. Axially, CO molar fractions were lower whereas NO molar fractions were higher when λ increased.

Secondly, air inlet temperature increased from 400 °C to 700 °C. It was seen that, the mean temperature was predicted approximately 70 °C higher. In case of species molar fractions, similar values were predicted for CO_2 and O_2 molar fractions, whereas there was some disparity in the vicinity of the burner. CO molar fractions reached almost three percent in the vicinity of the burner. Moreover, NO molar fractions increased dramatically with the increase of air inlet temperature.

Air nozzle size decreased from 10 mm to 7 mm in the last modification. This yielded decrease an increase of the air inlet velocity from 109 m/s to 223 m/s. As a consequence, the mean temperature decreased by about 55 °C. CO_2 and O_2 profiles vary in the vicinity of the burner. CO and NO predictions yield lower values of molar fractions.

Moreover, the contributions of the NO mechanisms were investigated. To sum up, N_2O path mechanism was observed to be the dominant mechanism in all cases. Thermal mechanism played a greater role when air inlet temperature was increased. Prompt mechanism appears to be insignificant regardless of changing the operating conditions. Furthermore, The NO predictions were strongly dependent on the way the O and OH concentrations are evaluated, on the way the N_2O concentration was calculated, and on how the pdf was prescribed to determine mean values.

Overall, the predictions are satisfactory for temperature fields and CO_2 and O_2 molar fractions. However, some discrepancies are observed in the vicinity of the burner especially for CO and NO molar fractions. In general, the deviation from the experimental data is not large although the accuracy of the model is limited.

According to the numerical analysis, OH contours of the cases show that OH intensity increases with higher air inlet temperature. However, the intensity decreases with the increase of excess air ratio. Additionally, the reaction zone moved towards the inlet when the excess air ratio was increased which is consistent with the past experimental work. Furthermore, OH intensity decreased significantly when air nozzle diameter increased.

This study includes the RANS simulations of a mild combustor. Better predictions can be achieved by using more detailed turbulence and combustion models. Although RANS approach is widely used in the industry, LES approach can be used to increase the accuracy of the predictions without increasing the computational cost dramatically as in the case of DNS. By means of extensive research, flameless oxidation can be a way to a cleaner and sustainable environment.

REFERENCES

1. World Energy Council, World Energy Resources 2013 Survey. (2013). London, England: World Energy Council.

2. Smith, P.B., Okoye, S.M., De Wilde, J. & Deshingkar, P. (2009). *World at the crossroads: Towards a sustainable, equitable and liveable world*. London, England: Routledge.

3. Tsuji, H., Gupta, A.K., Hasegawa, T., Katsuki, M., Kishimoto, K. & Morita, M. (2003). *High temperature air combustion.* London, England: CRC Press LLC.

4. Lackner, M., Winter, F. & Agarwal, A.K. (2010). *Handbook of combustion*. Hoboken, New Jersey, USA: John Wiley & Sons.

5. Poinsot, T. & Veynante, D. (2005). *Theoretical and numerical combustion, second edition*. Philadelphia, Pennsylvania, USA: Edwards.

6. Magnussen, B.F. (2005). The Eddy Dissipation Concept: A bridge between science and technology, in *ECCOMAS Thematic Conference on Computational Combustion*. Lisbon, Portugal.

7. Magnussen, B.F. (1983). A model for flame extinction in turbulent flows (EDC), in *Turbulent Shear Flows*. Karlsruhe, Germany.

8. Magnussen, B.F. (1981). On the structure of turbulence and a generalized Eddy Dissipation Concept for chemical reaction in turbulent flow, in *19th American Institute of Aeronautics and Astronautics Aerospace Science Meeting*. St. Louis, Missouri, USA.

9. Veríssimo, A.S., Rocha, A.M.A. & Costa M. (2013). Importance of the inlet air velocity on the establishment of flameless combustion in a laboratory combustor. *Experimental Thermal and Fluid Science*, vol. 44, pp. 75-81.

10. Li, G., Gutmark, E.J., Stankovic, D., Overman, N., Cornwell, M., Fuchs, L., & Vladimir M. (2006). Experimental study of flameless combustion in gas turbines combustors, in *44th AIAA Aerospace Sciences Meeting and Exhibit*. Reno, Nevada, USA.

11. Wünning, J.A., & Wünning, J.G. (1997). Flameless oxidation to reduce thermal NO formation. *Prog. Energy Combust.,* vol. 23, pp. 81-94.

12. Glassman, I., & Yetter, R.A. (2008). *Combustion, fourth edition*. Burlington, Massachusetts, USA: Elsevier.

13. Lefebvre, A.H. (1999). *Gas turbine Combustion, second edition*. Philadelphia, Pennsylvania, USA: Taylor & Francis.

14. Özdemir, B.I. & Peters, N. (2001). Characteristics of the reactions zone in a combustor operating at mild combustion. *Exp. Fluids,* vol. 30, pp. 683-695.

15. Orsino, S., Weber, R. & Bollettini, U.G.O. (2001). Numerical simulation of combustion of natural gas with high-temperature air. *Combustion Science and Technology*, vol. 170, pp. 1-34.

16. Galletti, C., Parente, A. & Tognotti, L. (2007). Numerical and experimental investigation of a mild combustion burner. *Combustion and Flame*, vol. 151, pp. 649-664.

17. Szegö, G., Dally, B. & Nathan, G. (2009). Operational characteristics of a parallel jet MILD combustion burner system. *Combustion and Flame*, vol. 156, pp. 429-438.

18. Guillou, E., Cornwell, M. & Gutmark, E. (2009). Application of flameless combustion for gas turbine engines, in *47th AIAA Aerospace Sciences Meeting Including The New Horizons Forum and Aerospace Exposition*. Orlando, Florida, USA.

19. Castela, M., Verissimo, A.S., Rocha, A.M.A. & Costa, M. (2012). Experimental study of the combustion regimes occurring in a laboratory combustor. *Combustion Science and Technology,* vol. 184, pp. 243-258.

20. Veríssimo, A., Oliveira, R., Coelho, P.J. & Costa M. (2012). Numerical simulation of a small-scale mild combustor*. Journal of Physics: Conference Series*, vol. 395, pp. 012003.

21. Veríssimo, A.S., Rocha, A.M.A. & Costa, M. (2013). Experimental study on the influence of the thermal input on the reaction zone under flameless oxidation conditions. *Fuel Processing Technology,* vol. 106, pp. 423-428.

22. Ferziger, J.H. & Perić, M. (2002). *Computational methods for fluid dynamics, third edition*. Berlin, Germany: Springer.

23. Shih, T.L., Liou, W.W., Shabbir, A., Yang, Z. & Zhu, J. (1995). A new k-epsilon eddy viscosity model for high Reynolds turbulent flows*. Computers and Fluids,* vol. 24, pp. 227-238.

24. Reynolds, W.C. (1987). Fundamentals of turbulence for turbulence modeling and simulation. *Lecture Notes for Von Karman Institute*, AGARD CP-93, NATO.

25. Shih, T.S., Zhu, J. & Lumley, J.L. (1995). A new Reynolds stress algebraic equation model. *Computer Methods in Applied Mechanics and Engineering,* vol. 125, pp. 287-302.

26. Magnussen, B.F. (1989). Modeling of pollutant formation in gas turbine combustors based on the Eddy Dissipation Concept, *in CIMAC Conference*. Tianjin, China.

27. Modest, B.F. (2013). Radiative heat transfer, third edition. *Amsterdam, The Netherlands: Elsevier*

28. Coppalle, A. & Vervisch, P. (1983). The total emissivities of high-temperature flames. *Combustion and Flame,* vol. 49, pp. 101-108.

29. Kuo, K.K., (2005). *Principles of combustion, second edition*. Hoboken, New Jersey, USA: John Wiley & Sons.

APPENDICES

Temperature Contours of the Cases

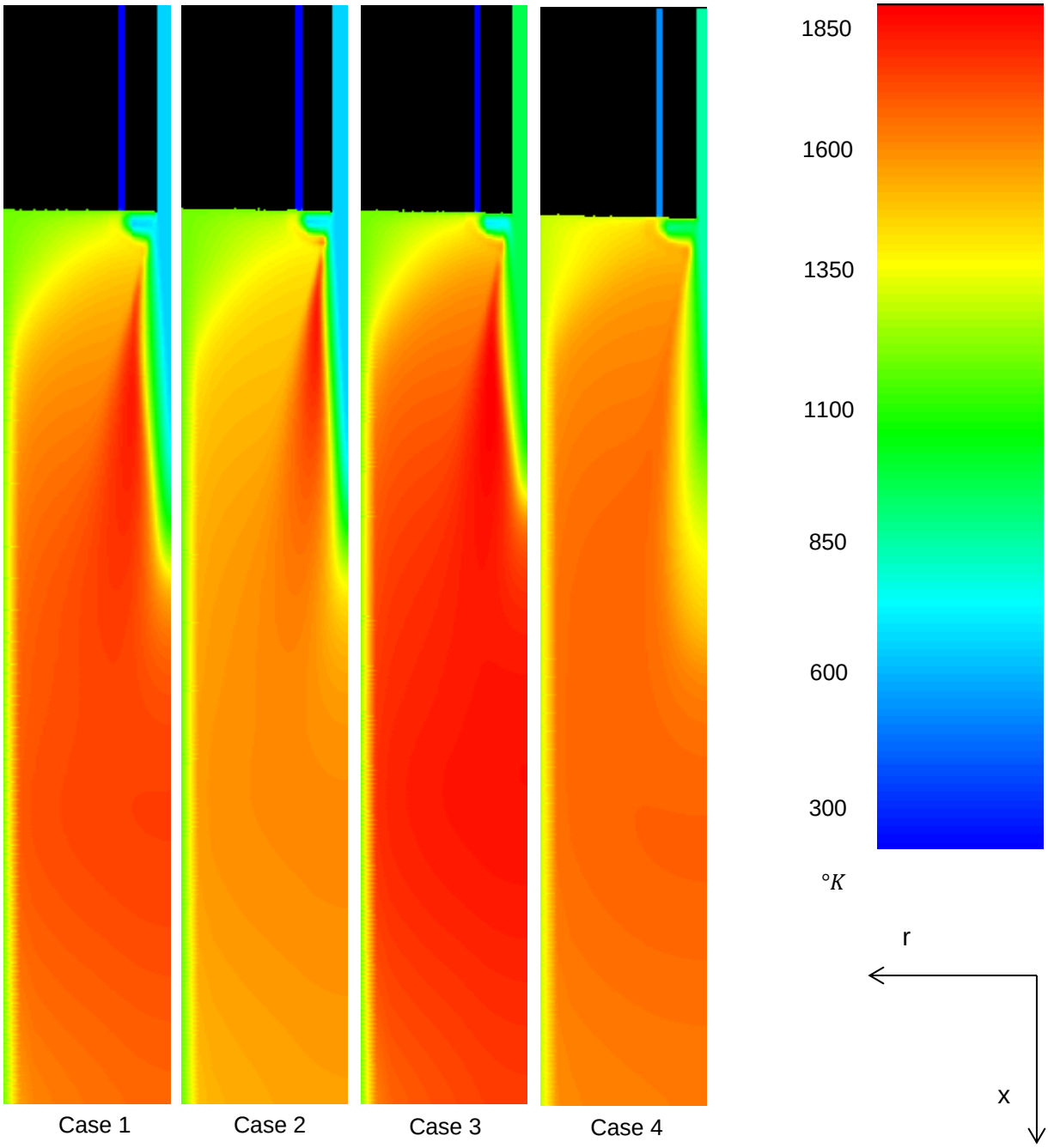

Dry CO_2 Mole Fraction Contours of the Cases

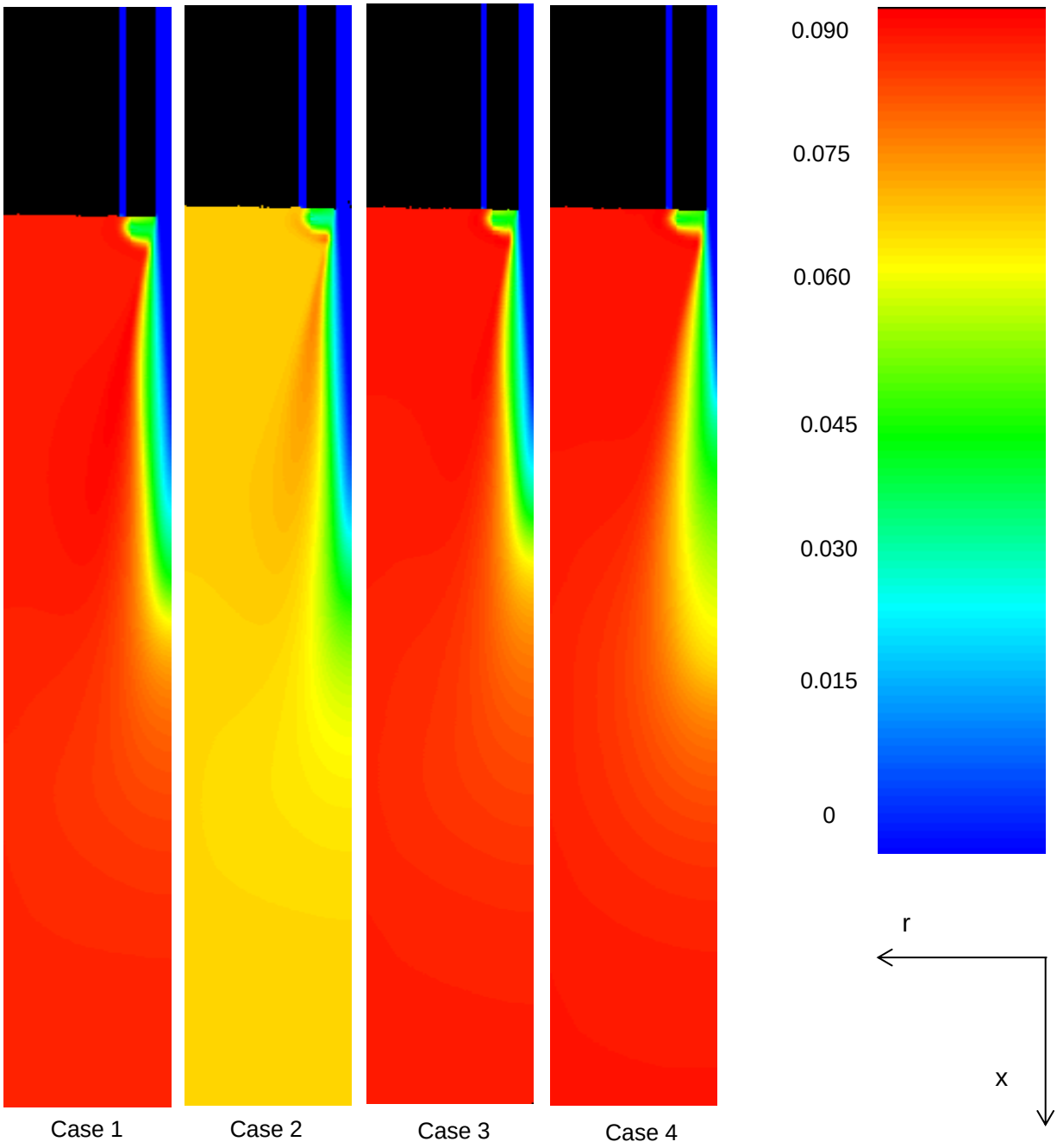

Dry O_2 Mole Fraction Contours of the Cases